



# Spinel Harzburgite-Derived Silicate Melts Forming Sulfide-Bearing Orthopyroxenite in the Lithosphere. Part 1: Partition Coefficients and Volatile Evolution Accompanying Fluid- and Redox-Induced Sulfide Formation

A. Bénard<sup>1\*</sup>, C. Le Losq<sup>2</sup>, O. Müntener<sup>1</sup>, M. Robyr<sup>1</sup>, O. Nebel<sup>3</sup>, R. J. Arculus<sup>4</sup> and D. A. Ionov<sup>5</sup>

<sup>1</sup>Institute of Earth Sciences, University of Lausanne, Lausanne, Switzerland, <sup>2</sup>Institut de Physique du Globe de Paris, Université de Paris Cité, Paris, France, <sup>3</sup>School of Earth, Atmosphere and Environment, Monash University, Clayton, VIC, Australia, <sup>4</sup>Research School of Earth Sciences, The Australian National University, Canberra, ACT, Australia, <sup>5</sup>Géosciences Montpellier, Université de Montpellier, Montpellier, France

## OPEN ACCESS

### Edited by:

Melissa Ovedia Anderson,  
University of Toronto, Canada

### Reviewed by:

Neil Bennett,  
University of Toronto, Canada  
Igor Victorovich Ashchepkov,  
V.S. Sobolev Institute of Geology and  
Mineralogy (RAS), Russia

### \*Correspondence:

A. Bénard  
antoine.benard@unil.ch

### Specialty section:

This article was submitted to  
Petrology,  
a section of the journal  
Frontiers in Earth Science

**Received:** 01 February 2022

**Accepted:** 19 April 2022

**Published:** 12 July 2022

### Citation:

Bénard A, Le Losq C, Müntener O,  
Robyr M, Nebel O, Arculus RJ and  
Ionov DA (2022) Spinel Harzburgite-  
Derived Silicate Melts Forming Sulfide-  
Bearing Orthopyroxenite in the  
Lithosphere. Part 1: Partition  
Coefficients and Volatile Evolution  
Accompanying Fluid- and Redox-  
Induced Sulfide Formation.  
Front. Earth Sci. 10:867979.  
doi: 10.3389/feart.2022.867979

We report abundances of major trace and volatile elements in an orthopyroxenite vein cutting a sub-arc, mantle-derived, spinel harzburgite xenolith from Kamchatka. The orthopyroxenite contains abundant sulfides and is characterized by the presence of glass (formerly melt) both interstitially and as inclusions in minerals, comparable with similar veins from the West Bismarck arc. The glass formed by quenching of residual melts following crystallization of abundant orthopyroxene, amphibole, and minor olivine and spinel. The interstitial glass has a low-Ti, high-Mg# andesite composition, with a wide range of H<sub>2</sub>O and S contents but more limited F and Cl variations. We calculate trace element partition coefficients using mineral and glass data, including those for halogens in amphibole, which agree with experimental results from the literature. Despite having a similar, high-Mg# andesite composition, the orthopyroxene-hosted glass inclusions usually contain much more H<sub>2</sub>O and S than the interstitial glass (4–7 wt% and ~2,600 ppm, respectively). The initial vein-forming melts were oxidized, recording oxygen fugacity conditions up to ~1.5 log units above the fayalite–magnetite–quartz oxygen buffer. They intruded the sub-arc mantle lithosphere at ≥1,300°C, where they partially crystallized to form high-Mg# andesitic derivative melts at ca. 1,050–1,100°C. Comparison with literature data on glass-free orthopyroxenite veins from Kamchatka and the glass-bearing ones from West Bismarck reveals fundamental similarities indicating common parental melts, which were originally produced by low-degree melting (≤5%) of spinel harzburgite at ≥1,360°C and ≤1.5 GPa. This harzburgite source likely contained ≤0.05 wt% H<sub>2</sub>O and a few ppm of halogens. Volatile evolution inferred from glass compositions shows that (i) redox exchange between S<sup>6+</sup> in the original melt and Fe<sup>2+</sup> in the host mantle minerals, together with (ii) the formation of an S-bearing, (H<sub>2</sub>O, Cl)-rich hydrothermal fluid from the original melt, provides the conditions for the formation of

abundant sulfides in the orthopyroxenites during cooling. During this process, up to 85% of the original melt S content (~2,600 ppm) is locally precipitated as magmatic and hydrothermal sulfides. As such, melts derived from spinel harzburgite sources can concentrate chalcophile and highly siderophile metals in orthopyroxenite dykes and sills in the lithosphere.

**Keywords:** sub-arc mantle, low-Ca boninite, harzburgite, partial melting, volatile, halogen, sulfur, pyroxenite

## INTRODUCTION

The term boninite is used to characterize mantle-derived magmas of magnesian, basaltic andesite, and andesite compositions ( $\geq 52$  wt%  $\text{SiO}_2$  and  $\geq 8$  wt%  $\text{MgO}$  in the most primitive end-members), which have distinctively low- $\text{TiO}_2$  ( $\leq 0.5$  wt%) and alkali ( $\leq 2$  wt%  $\text{Na}_2\text{O} + \text{K}_2\text{O}$ ) contents (Crawford et al., 1989; Le Bas, 2000). Although these two compositional proxies are believed to trace depleted mantle sources, the term boninite covers a continuum of magma compositions and conditions of melt generation (Falloon and Danyushevsky, 2000). This issue was partly addressed by using a  $\text{CaO}/\text{Al}_2\text{O}_3$  discriminant of 0.75, believed to primarily indicate the transition from spinel lherzolite to spinel harzburgite sources consequent to the elimination of clinopyroxene from the residue (Crawford et al., 1989). This threshold distinguishes high-Ca ( $\text{CaO}/\text{Al}_2\text{O}_3 > 0.75$ ) from low-Ca boninites (LCBs;  $\text{CaO}/\text{Al}_2\text{O}_3 < 0.75$ ). A more recent classification by Pearce and Reagan (2019) connects clinopyroxene saturation or undersaturation during mantle melting to the  $\text{SiO}_2$  enrichment of boninites, distinguishing low- $\text{SiO}_2$  boninites (lherzolite source) from high- $\text{SiO}_2$  boninites (harzburgite source) (Umino et al., 2015; Pearce and Arculus, 2021; Valetich et al., 2021).

Magmas classified as boninites (particularly LCBs) are relatively rare rock types and are usually found at convergent plate margins. All LCBs are depleted in moderately incompatible heavy rare-earth elements (HREEs), which contrast with frequent, although variable, enrichments in the highly incompatible large-ion lithophile elements (LILE) or light REEs (LREEs), often producing primitive mantle-normalized, U-shaped patterns. The canonical views imply that these signatures originate from partial melting of prior melt-depleted mantle sources at low pressure ( $\leq 2$  GPa), triggered by the ingress of a mobile component (“flux-melting”) derived by the devolatilization and/or partial melting of subducted oceanic lithosphere (“slab”; Jenner, 1981; Hickey and Frey, 1982; Cameron et al., 1983; Umino and Kushiro, 1989; Taylor et al., 1994; Bédard, 1999; Kamenetsky et al., 2002; Reagan et al., 2009; König et al., 2010). Elevated  $\text{H}_2\text{O}$  and halogen contents in some boninites, found either as lavas (Sobolev and Chaussidon, 1996; Li et al., 2022) or as quenched melts in mantle rocks (sub-arc peridotites; Bénard et al., 2016; 2017a; 2018a), are consistent with the critical involvement of a volatile-rich, slab component.

The classical models of boninite petrogenesis consider the two end-members (i.e., high Ca–low  $\text{SiO}_2$  and low Ca–high  $\text{SiO}_2$ ) as being formed within a continuum where mantle melting proceeds within the clinopyroxene stability field and possibly extends

beyond the exhaustion of this mineral in the residues, and wherein orthopyroxene melts incongruently (e.g., König et al., 2010). All of these models are based on the inversion of boninite chemical characteristics to infer the nature of their respective mantle sources. More recently, however, new information has been gained from direct detailed studies of mantle peridotites from the Kamchatka (Bénard and Ionov, 2012, 2013) and West Bismarck (Papua New Guinea; Bénard et al., 2018a) arcs, both containing sulfide-bearing orthopyroxenite veins, which in the case of the second locality are characterized by the presence of sulfide-bearing glass. It has been shown that these veins formed from LCB magmas, producing high- $\text{Mg}\#$  (with  $\text{Mg}\# = \text{Mg}/[\text{Mg} + \text{Fe}_t]$ , where  $\text{Fe}_t$  indicates all Fe treated as  $\text{Fe}^{2+}$ ) andesitic derivatives through fractional crystallization (Bénard and Ionov, 2012, 2013; Bénard et al., 2018a). Petrological modeling was used to argue that low-degree ( $\leq 5\%$ ), partial melting of refractory (prior melt-depleted) spinel harzburgite can occur as an independent, second-stage event rather than in a melting continuum (Bénard et al., 2018a). Aggregating low-volume harzburgite-derived melts to a larger batch of lherzolite-derived liquids (i.e., implying elevated total melting degrees) leads to major element compositions of the bulk magmas, which are significantly distinct from those produced through a low-degree, second-stage melting process of harzburgite only (Duncan and Green, 1987; Klingenberg and Kushiro, 1996; Falloon and Danyushevsky, 2000; Bénard et al., 2018a).

A fundamental question linked to our understanding of LCB petrogenesis concerns highly and moderately incompatible element concentration processes during melt generation in the mantle, such as for some volatiles or  $\text{Fe}^{3+}$ , respectively. For example, assuming a low-degree, second-stage melting process, the spinel harzburgite sources of the parental melts forming West Bismarck orthopyroxenite veins should only contain 0.01–0.05 wt %  $\text{H}_2\text{O}$  (Bénard et al., 2018a). Such low abundances overlap those expected in the mantle sources of mid-ocean ridge basalts (Saal et al., 2002; Salters and Stracke, 2004) and are thus difficult to reconcile with a flux-melting process for generating these LCBs. However, the behavior of other volatiles such as halogens (F and Cl) and sulfur (S) during low-degree, second-stage melting processes is poorly constrained. One fundamental issue is the sulfide saturation state and how it evolves from mantle sources to magma emplacement. Second-stage melting has notably been proposed as key for triggering sulfide undersaturation during melt generation in the mantle, allowing for the chalcophile and highly siderophile element abundances to concentrate in the evolving melts during the early stages of crystal fractionation (Hamlyn and Keays, 1986; Keays, 1995). Regarding the

sulfide-rich nature of orthopyroxenite veins, a range of 2–3 orders of magnitude was estimated for oxygen fugacity conditions ( $fO_2$ ), extending from  $-1$  to  $+1.5$  log units relative to the fayalite–magnetite–quartz (FMQ) oxygen buffer ( $-1 \leq \Delta \log fO_2[\text{FMQ}] \leq +1.5$ ; Bénard et al., 2018a). This  $fO_2$  range typically corresponds to the transition from  $S^{2-}$  to  $S^{6+}$  in silicate melts (Jugo et al., 2010), which leaves considerable uncertainties on the real nature and extent of sulfur transport in LCBs.

In the first article of this two-part study, we report a detailed account of the abundances of major and lithophile trace elements and volatiles ( $H_2O$ , F, Cl, and S) in a sulfide- and glass-bearing orthopyroxenite vein cutting a sub-arc mantle xenolith from Kamchatka. We compare the results to those from Bénard and Ionov (2012, 2013) and Bénard et al., (2018a), with an emphasis on volatile behaviors ( $H_2O$ , F, and Cl) and the evolution of the sulfide saturation state. In the second article, these results will be extended to new analytical data for vein sulfide compositions, including major base metals as well as chalcophile and highly siderophile trace elements.

## MATERIALS AND METHODS

### Electron-Probe Micro-analysis

Major element compositions of silicate minerals and glasses were determined in a polished thick ( $\sim 120 \mu\text{m}$ ) section by wavelength-dispersive (WDS) electron-probe micro-analysis (EPMA) using a CAMECA SX100 instrument at the Research School of Earth Sciences at the Australian National University (ANU, Australia), and a JEOL 8530-F field-emission instrument at the Institute of Earth Sciences of the University of Lausanne (UNIL, Switzerland). Mineral analyses were performed at an accelerating voltage of 15 kV and a sample current of 20 nA (focused beam routine). Glass analyses were performed with a defocused beam ( $5\text{--}10 \mu\text{m}$ ) and at a reduced sample current of 2–8 nA, with Na and K analyzed first with reduced counting times to minimize the loss or migration of alkali metals. Sulfur was the last element determined during glass analyses at ANU, using two spectrometers (PET and LPET) and a sample current of 100 nA. Counting times at ANU were 5–10 s on the background, and 120 s (S), 20 s (Cr and Ni), 15 s (Ca and Ti), and 10 s for all other elements on peak. Counting times at UNIL were 5–10 s on the background and 10–20 s on peak for Na and K, and 15 and 30 s for all other elements. Matrix effects were corrected using Phi ( $\rho$ )  $z$  modeling available on Peak Sight<sup>®</sup> software from CAMECA<sup>™</sup> at ANU and using the Armstrong PRZ oxide correction at UNIL. The positions of the element peaks were checked at least every 10 analyses. Mineral and glass (VG-2; Jarosewich et al., 1980) standards were analyzed either daily or at the start and end of each analytical session to estimate analytical drift, which was negligible. Major element maps were collected at ANU at an accelerating voltage of 15 kV and an increased sample current of 40 nA. Some of the maps were collected with a Bruker<sup>™</sup> energy-dispersive spectrometer (EDS) coupled to the SX100 instrument.

Amphibole analyses at UNIL were performed with a defocused beam ( $10 \mu\text{m}$ ) at an increased sample current of 40 nA, and with

counting times of 5 s (background) and 10 s (peak) for Cr, 10 and 20 s for Ca, Na, and K, and 15 and 30 s for all other elements, except for halogens. Fluorine and chlorine analyses in amphibole were performed using a method similar to that described in Bénard et al. (2017a), with F being simultaneously analyzed on a TAP and two TAPL spectrometers to increase counting times and avoid Fe  $L_{\alpha}$  tail overlapping on F  $K_{\alpha}$ . The total counting times were 300 s for F and 100 s for Cl, both on peak and background. This analytical protocol resulted in a significant decrease of the detection limits (down to  $\sim 100$  ppm for F and  $\sim 30$  ppm for Cl on the JEOL 8530-F instrument) relative to a conventional setup (typically 650–800 ppm for F and 200–250 ppm for Cl). Primary standards used for peak positioning and intensity calibration were F-phlogopite for F (9.02 wt% F) and scapolite for Cl (1.43 wt% Cl). The calibration was tested daily against VG2 basaltic glass secondary standard ( $220 \pm 66$  F and  $306 \pm 13$  Cl; Jarosewich et al., 1980) and mantle-derived vein amphibole from Kamchatka, for which both EPMA and secondary-ion mass spectrometry data have already been reported (e.g., with F ranges between  $\sim 1,500$  and  $5,000\text{--}6,000$  ppm; Bénard et al., 2017a).

The same analytical protocol as for amphibole was used to analyze F in glass with a  $10\text{--}20 \mu\text{m}$  beam and matrix effects corrected using compositions previously acquired with the glass routine described before. No halogen loss, either through devolatilization or migration from below the beam within the glass, was observed during those analyses, demonstrating that the method is valid for the glass compositions in this study (**Supplementary Figure S1**).

### Scanning Electron Microscopy

Back-scattered electron (BSE) images and semi-quantitative phase analyses at high spatial resolution were acquired using a Tescan MIRA II LMU field-emission scanning electron microscope (SEM) at UNIL. *In situ* analyses were performed on this instrument by EDS using a PentaFET 3x X-ray detector. BSE images were acquired at a working (sample) distance of 9 mm, an accelerating voltage of 20 kV, and a sample current of  $\sim 0.5$  nA, allowing a spatial resolution (spot size) of  $\sim 5$  nm. EDS analyses were performed at a working distance of 20–23 mm and with an increased sample current of 0.9–1.3 nA to maximize count rates, leading to a spatial resolution of 6–7.5 nm. Acquisition parameters included an energy step of 20 eV, a process time of 5 s to increase the signal-to-background ratio and spectral resolution, and an acquisition time of 1 min per analysis. Data treatment was made using the Oxford Instruments AZtec software packaging.

### Laser Ablation Inductively Coupled Plasma Mass Spectrometry

Lithophile trace element abundances in vein minerals and glass were determined in the thick section by laser ablation inductively coupled plasma mass spectrometry (LA-ICPMS) at ANU. This system comprises a UV ( $\lambda = 193$  nm) excimer laser (Lambda Physik CompEx 110) and an ANU-designed HelEx ablation cell coupled to an Agilent 7700x quadrupole ICPMS. Analyses were performed with a laser set at a 5-Hz pulse rate, 29.5 kV, 50 mJ,

and using 50 or 100  $\mu\text{m}$  beam diameters. For each laser ablation run,  $\sim 25$  s were counted on the carrier gas (background) followed by  $\sim 35$  s for signal. The NIST 610 glass standard was used for calibration (Jochum et al., 2011), with  $^{29}\text{Si}$  chosen as the internal standard (with the abundances determined by EPMA). The accuracy and precision of the method were assessed by calculating  $1\sigma$  RSD from replicate analyses of BCR-2G reference material during the runs (Gao et al., 2002; Jochum et al., 2005). For each analysis, we carefully avoided the ablation of inclusions, exsolutions, or cracked areas by optical checks prior to ablation. The signal was further filtered to eliminate any eventual heterogeneity bias during data processing, using an in-house Excel spreadsheet following the method of Longgerich et al. (1996).

## Raman Microspectroscopy

The dissolved  $\text{H}_2\text{O}$  contents in glasses were measured using confocal Raman microspectroscopy at the Paris Institute of Earth Physics, University of Paris (IPGP, France). The Raman spectra of the glasses were recorded with a LabRAM HR Evolution spectrometer, equipped with a Peltier-cooled CCD and 1800 lines  $\text{mm}^{-1}$  grating. The samples were excited with a Coherent MX solid-state laser ( $\lambda = 488$  nm) focused through a  $\times 50$  Olympus objective on the sample surface. The confocal aperture of the spectrometer was set to 30. With this setup, spectral resolution was  $\sim 3$   $\text{cm}^{-1}$  and spatial resolution was  $\leq 1$   $\mu\text{m}$ . All spectra were recorded with the laser focused at 3–5  $\mu\text{m}$  below the sample's surface to avoid any surface effects (Schiavi et al., 2018). The laser power on the sample was measured as equal to  $\sim 10$  mW with this setup. Potential damage of the samples was checked by recording several spectra on the same spot and varying laser power, without the identification of any effect.

The  $\text{H}_2\text{O}$  contents of the glasses were retrieved from 1) the internal calibration protocol defined in Le Losq et al. (2012) and 2) an external calibration method, following Behrens et al. (2006) and Schiavi et al. (2018). The internal calibration method of Le Losq et al. (2012) allowed measurements that are independent of the spectrometer setup and glass chemical composition. The external calibration method allowed cross-validation of the values determined with the internal calibration, following the practice adopted in Bénard et al. (2018a). For both methods, glass standards include those from Le Losq et al. (2012) and Ca-bearing alumino-silicate hydrous glasses with known  $\text{H}_2\text{O}$  contents ranging from 0.2 to 8 wt% (Le Losq et al., 2017). Raman data treatment was performed using Python programming software, with the *rampy* open-source software library (Le Losq, 2018).

## RESULTS

### Petrographic Observations

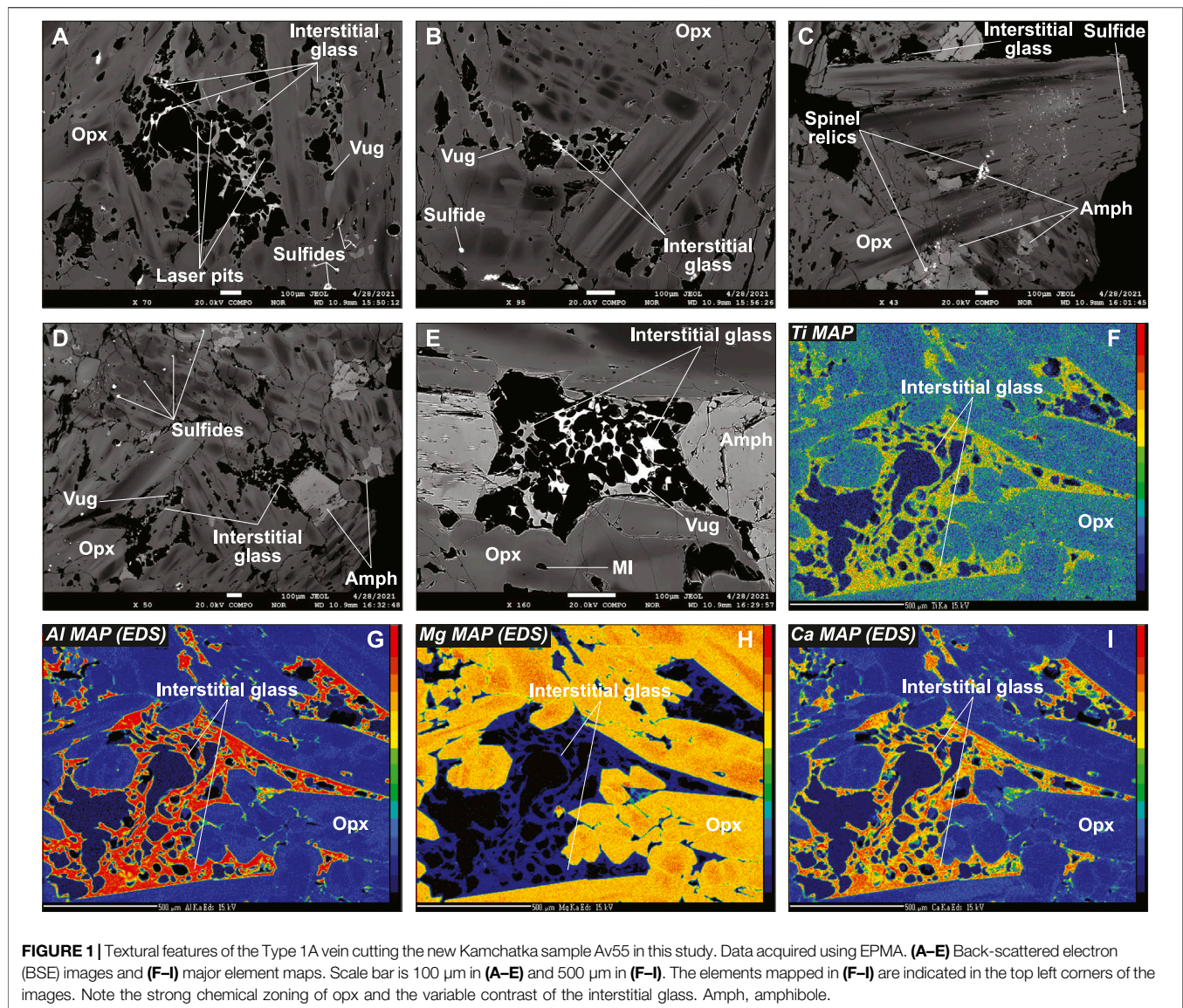
The complete dataset supporting this study is reported in **Supplementary Table S1**. The new sample in this study (Av55) was collected on the active Avacha volcano in the southern part of the Kamchatka peninsula (Russian Federation). It was found in volcanic ash and scoria of low-K basaltic andesite and andesite compositions on the western slope of Avacha facing Koryaksky volcano, together with the samples

from the same collection described in Ionov (2010), Bénard et al. (2011), Ionov et al. (2011), Bénard and Ionov (2012, 2013), and Bénard et al. (2016, 2018c). More details on the geology of the region and the overall tectonic setting can be found in those studies.

The host rock of the orthopyroxenite vein in this study is a predominantly coarse-grained spinel harzburgite with protogranular micro-structures outlined by olivine and spinel, which are typical textural features for peridotites from the sub-arc mantle lithosphere (**Supplementary Figures S2–S5**; McInnes et al., 2001; Ionov, 2010; Ionov et al., 2011, 2013; Bénard et al., 2017b, 2021). Host spinel occurs as coarse or fine grains (**Supplementary Figure S2**). Former coarse orthopyroxene (opx) from the host appears as pseudomorphs entirely re-crystallized as anhedral fine grains of predominantly opx with minor clinopyroxene (cpx) and amphibole, which all contain minute spinel inclusions (**Supplementary Figures S2, S4**).

The orthopyroxenite vein displays irregular contacts with its host harzburgite, while grain coarsening and glass enrichment trends are identified from the contact toward the interior of the vein (**Supplementary Figures S3, S5**). As such, the vein contact can be considered as a “fringe,” a chilled margin likely formed by faster cooling rates with possible reaction with the host olivine (melt consumption is attested by the absence of glass). We use this textural feature to categorize the vein as “rapidly crystallized” (i.e., fringe-bearing; “Type 1A”) following previously established classifications (e.g., Bénard and Ionov, 2012, 2013). Small euhedral olivine grains were identified in the vein using EDS, but they are extremely rare (**Supplementary Table S1**). Vein opx is generally euhedral and systematically shows strong core-to-rim zoning and, much less frequently, oscillatory or irregular zoning (**Figures 1A–D** and **Supplementary Figure S6**). Minor amphibole, without any apparent zoning patterns, is either found as euhedral grains neighboring glassy areas or as an anhedral reaction product from former coarse spinel from the host (**Figures 1A–D**, **Supplementary Figures S7, S8**). Smaller spinel grains can occur not only as subhedral to euhedral inclusions in opx (**Supplementary Figure S9**) but also as anhedral host relics (isolated or as trails) in the same mineral, which are sometimes associated with traces of replacing amphibole (**Figure 1C** and **Supplementary Figure S5**). EDS analysis allows identifying these subhedral to euhedral spinels as chromite (**Supplementary Figure S9**). Small, rounded sulfide inclusions are frequent in vein opx (**Figure 1** and **Supplementary Figure S6**) but are more abundant in the fringes than in the central part of the vein (**Supplementary Figures S3, S8**).

A distinctive feature of the Kamchatka vein in this study when compared with earlier studies of Type 1A veins from this locality (Bénard and Ionov, 2012; 2013) is that it contains silicate glass, the proportion of which increases from the fringes toward the central part of the vein (**Supplementary Figure S5**). Glassy areas in the central part of the vein contain abundant vugs with curvilinear borders (**Figure 1** and **Supplementary Figure S6**). These vugs are frequently bordered by a coating, identified as Fe oxyhydroxide ( $\text{FeO}(\text{OH})$ ) by EDS, while clusters of small sulfides or isolated larger sulfide globules are found in the glass (**Supplementary Figure S9**). Fe oxyhydroxide also appears as

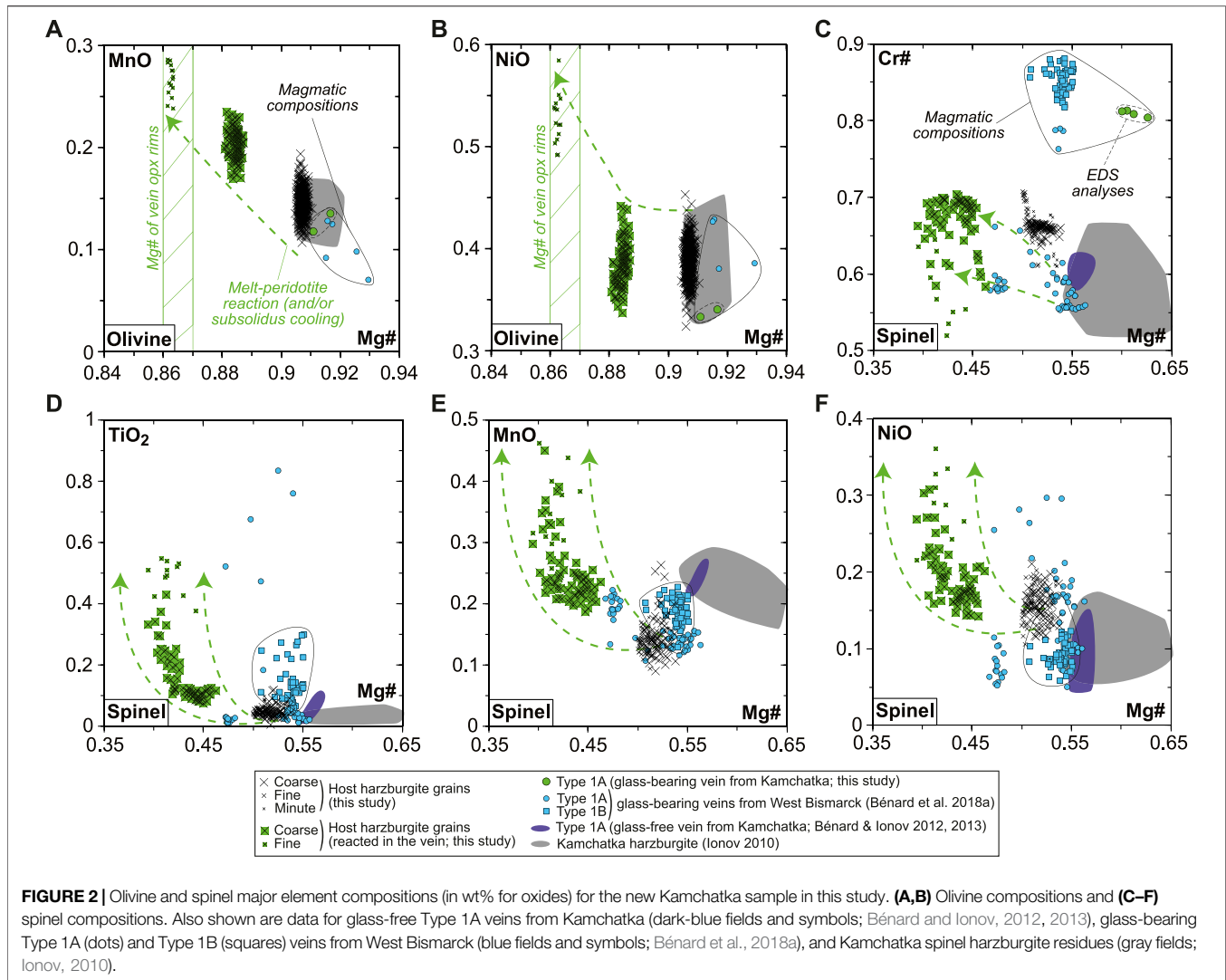


a post-magmatic replacement product of some sulfide inclusions in opx (**Supplementary Figure S9**). Another feature, absent from other Kamchatka vein samples, is the occurrence of abundant glass (formerly melt) inclusions (hereafter referred to as MIs), which are enclosed in opx and, more rarely, in amphibole (**Figure 1E**, **Supplementary Figures S6, S7, S10**). Only opx-hosted MIs were investigated in this study. Many of these MIs contain vugs, some contain sulfides, and a few contain visible daughter silicate crystals with euhedral shapes (**Supplementary Figure S10**). These have been identified by EDS analysis as amphibole (**Supplementary Figure S9**). A striking feature observed through BSE imaging is the varying contrast among all glassy areas, with darker MIs and lighter interstitial glass, although significant variations exist within the two groups (**Figures 1A–E**, **Supplementary Figures S6, S8, S10**). Variable BSE contrast is most likely imposed by fluctuating compositional parameters. However, whereas major element mapping confirms grain-scale

compositional variations in vein opx, the interstitial glass appears homogeneous (**Figures 1F–I**).

### Major and Lithophile Trace Elements

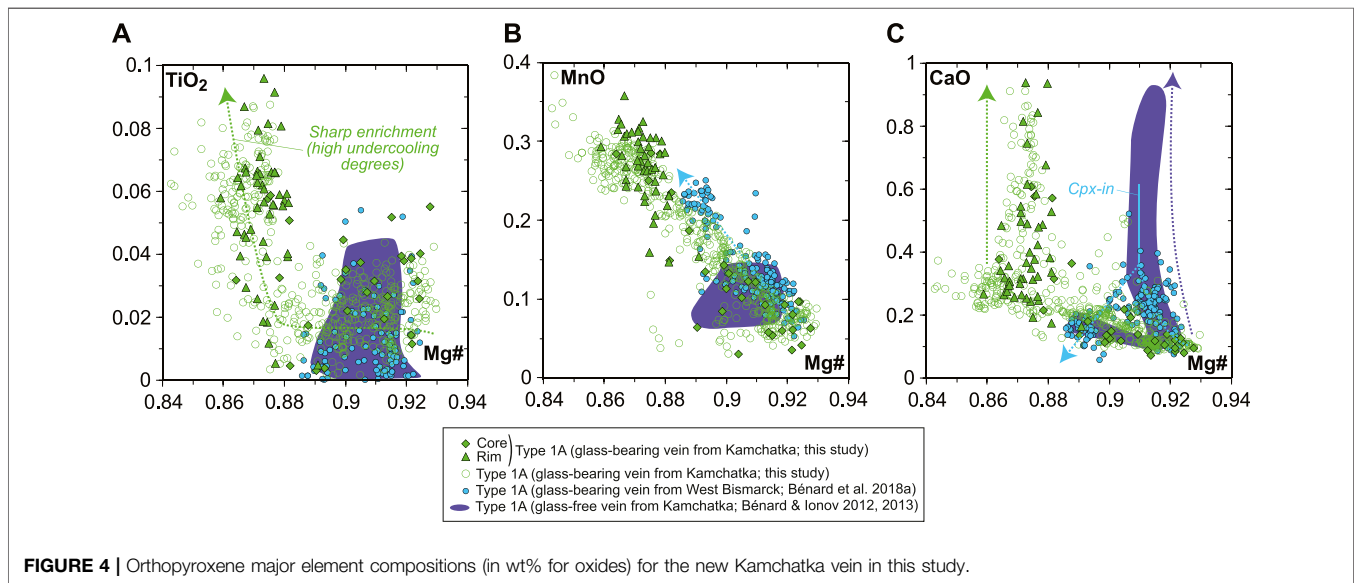
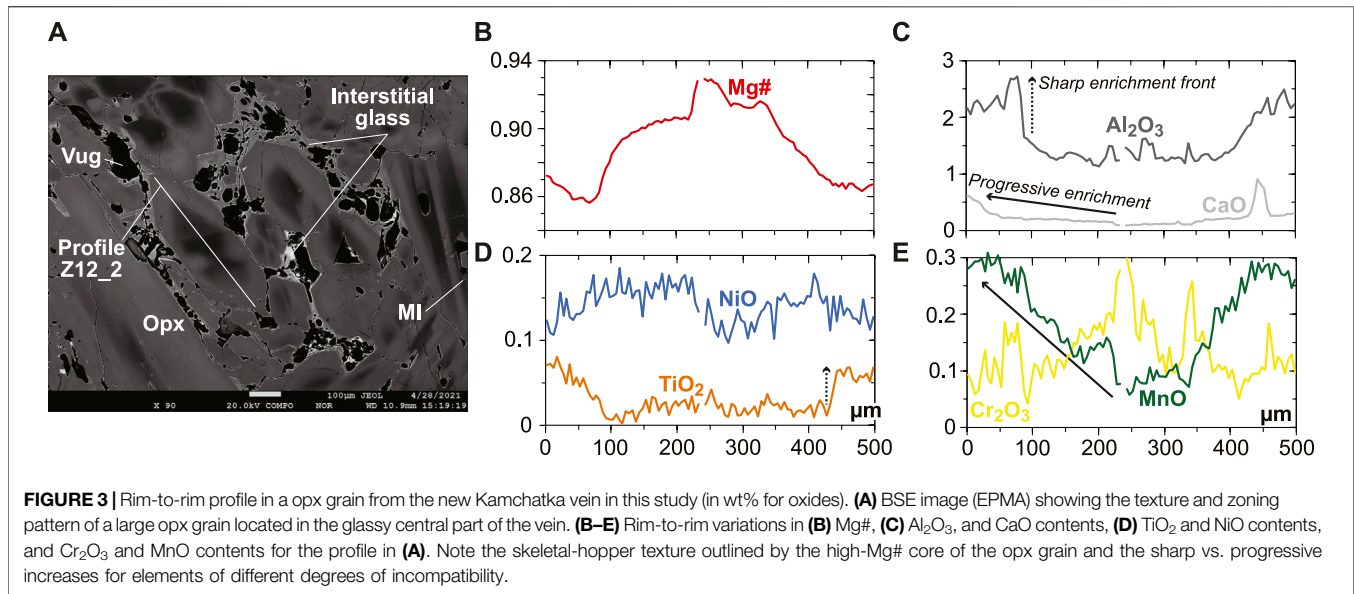
The BSE images and mapping suggest solid-state element diffusion in host olivine neighboring the vein, which is confirmed by EPMA profiles with homogeneous host olivine far from the vein but decreasing Mg# (from  $\sim 0.91$  to  $\sim 0.86$ ) and increasing MnO (from  $\sim 0.15$  to  $\sim 0.3$  wt%) and NiO (from  $\sim 0.4$  to  $\sim 0.5$  wt%) contents toward the vein fringes (**Supplementary Figure S3**). Similar “reacted” compositions are observed for rounded olivine relics, either isolated in the vein fringes or in fragments of the host harzburgite trapped within the branching vein (**Supplementary Figure S3**). Taken collectively, a melt-rock reaction trend is identified with olivine compositions, wherein Mg# decreases from the values of 0.91–0.92, typical of spinel harzburgite residues previously identified using Avacha mantle



xenoliths (e.g., Ionov, 2010), to  $\sim 0.86$  (Figures 2A,B). A similar trend is observed for spinel, given that Mg# in reacted spinel decreases from host harzburgite values, whereas Cr# (with  $\text{Cr\#} = \text{Cr}/[\text{Cr} + \text{Al}]$ ),  $\text{TiO}_2$ , MnO, and NiO increase (Figures 2C–F). This trend is confirmed by core-to-rim zoning patterns in former, coarse spinel from the host, now reacted to vein amphibole (Supplementary Figure S7). Despite being recrystallized as fine grains, host opx compositions are homogeneous and similar to that in other spinel harzburgite residues previously studied using Avacha mantle xenoliths, as do the host cpx (Supplementary Figure S4; Ionov, 2010).

The rare, euhedral olivine grains from the vein tend to have higher Mg# than in the host harzburgite (0.915–0.92; Figure 2A). Small euhedral vein chromite analyzed by EDS has much higher Mg# (0.60–0.63) and Cr# ( $\sim 0.81$ ) than host relics (Figure 2C). Vein opx display outstanding zoning features, some of which are outlined by former, skeletal-hopper grain shapes (Figure 3A), and the most common of which are “normal” patterns with a core-to-rim decrease of Mg# from  $\sim 0.93$  to  $\sim 0.86$  (i.e., similar to

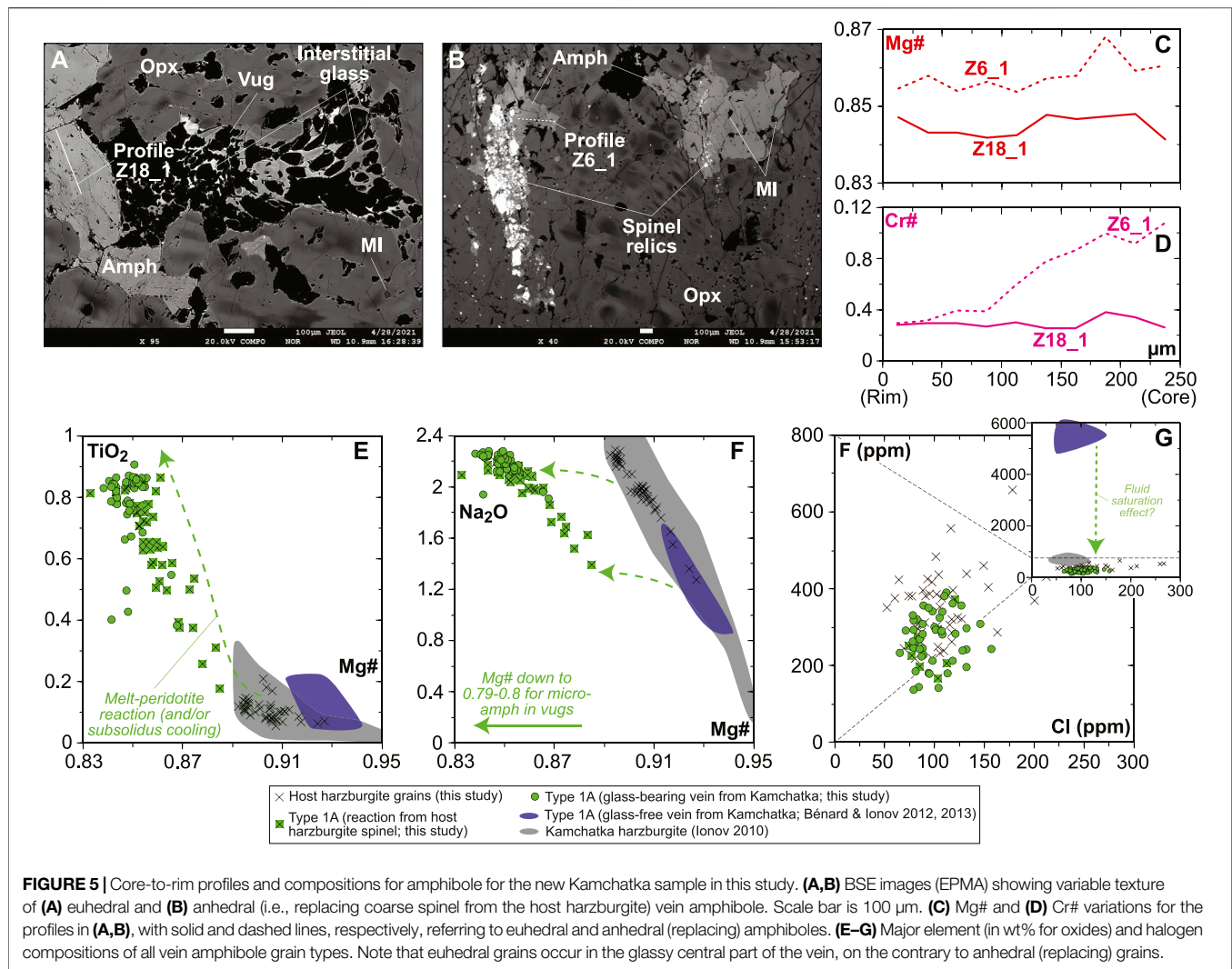
the low-Mg# host olivine relics in the vein; Supplementary Figure S3). This Mg# decrease is generally accompanied by increasing  $\text{TiO}_2$ , MnO, and CaO and decreasing  $\text{Cr}_2\text{O}_3$  and NiO (Figures 3B–E and Supplementary Figure S6). No “reverse” zoning patterns were observed with the notable exception of  $\text{Cr}_2\text{O}_3$ ; instead, normal patterns are commonly shifted toward lower Mg# values with consistent variations in the other elements (Supplementary Figure S6). Taken collectively, these data define clear covariation trends, for instance, a core-to-rim increase of  $\text{TiO}_2$ , MnO, and CaO against decreasing Mg#, with the visible effects of sharp enrichment fronts at grain rims for  $\text{TiO}_2$  and CaO (Figures 4A–C). Vein amphibole (mainly magnesio-hornblende), either found as euhedral grains or replacing spinel, was also investigated for core-to-rim chemical variations (Figures 5A–D and Supplementary Figure S8). Mg# generally decreases (0.89–0.83) with increasing  $\text{TiO}_2$  and  $\text{Na}_2\text{O}$ , replacing amphibole being intermediate in Mg# between the host and the euhedral examples (Figures 5E,F). Some Cr# variations



were only observed in the replacing amphibole with higher Cr# close to coarse spinel relics from the host (**Figure 5D** and **Supplementary Figure S8**). F and Cl range at 200–400 and 100–150 ppm, respectively, in all vein amphibole grains (**Figure 5G**). Glass compositions (normalized on an anhydrous basis) are illustrated in **Figure 6**, together with mineral–glass relationships. Interstitial glass has a limited compositional range, in agreement with mapping evidence; it has a low TiO<sub>2</sub> ( $\leq 0.4$  wt%; **Figure 6A**), intermediate to magnesian (2–4 wt% MgO; **Figure 6B**) andesite composition with small variations in CaO (7–9 wt%; **Figure 6C**). This composition can also be labeled as “high-Mg# andesite” according to its Mg# of 0.45–0.6 (**Figure 6D**) and following the classification of Kelemen et al. (2014). Melt inclusions display a very similar geochemical affinity but span a

wider compositional range extending to high-Mg# dacite, which has lower CaO contents than the andesite (**Figures 6A–D**). While the Mg#, CaO, and Al<sub>2</sub>O<sub>3</sub> relationships between coexisting opx rims and interstitial glass are consistent with experimental equilibrium values (Bédard, 2007; Waters and Lange, 2017), this is apparently less the case for amphibole rims (**Figure 6E**; Nandedkar et al., 2016).

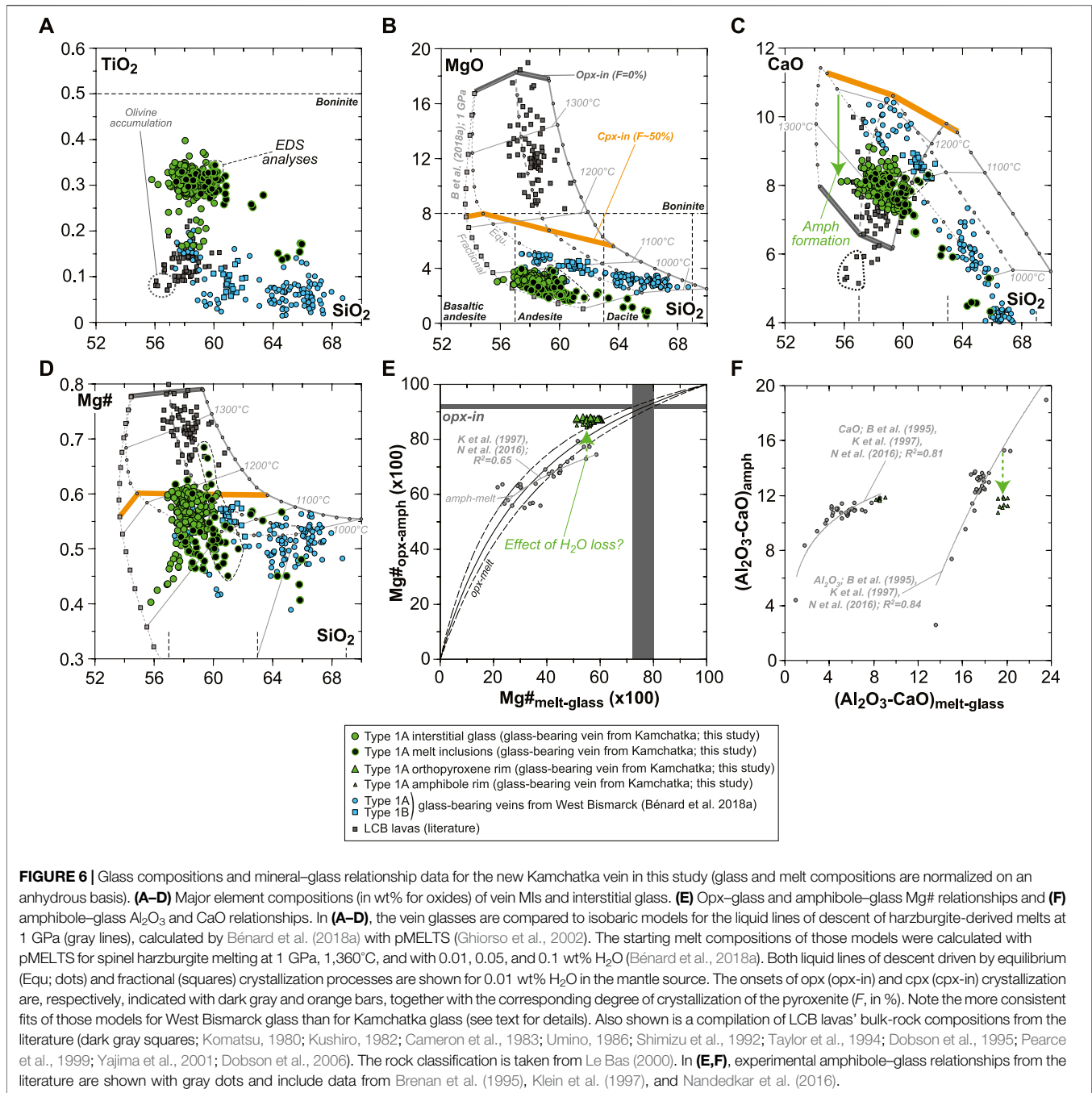
Primitive mantle-normalized patterns (PM; McDonough and Sun, 1995) for lithophile trace element abundances in vein opx are consistent whatever the laser spot size is, but only data acquired using a 50  $\mu\text{m}$  beam allowed the analysis of high-Mg# cores without the effects of zoning (**Figures 7A,B**). Pronounced core-to-rim trace element enrichments (by a factor of ca. 2–5 for a given grain) are correlated with the



decrease in Mg#; starting from the most depleted compositions, the overall level of enrichment for all vein opx grains investigated here reaches an order of magnitude (**Figures 7A, B**). Much less pronounced core-to-rim zoning is observed for vein amphibole, with HREEs ranging mostly between  $\sim 7$  and  $\sim 10$  times primitive mantle values (**Figure 7C**). The glass composition is homogeneous within the vein, which is characterized by slightly sinusoidal and LREE-enriched REE patterns, strong depletions in some of the high-field strength elements (HFSE; Nb, Ta, and Ti), and relative enrichments or positive spikes in some LILE (Cs, Rb, Ba, and Pb) or fluid-mobile elements (U; **Figure 7D**). The REE partitioning relationships between grain rims and glass are generally consistent with experimental equilibrium values for andesitic melt compositions, both in the case of opx and amphibole (**Figures 7E, F**; Bédard, 2007; Nandedkar et al., 2016). This consistency also persists for HFSE partitioning between amphibole and glass, but not for the most incompatible LILE (**Supplementary Table S1**).

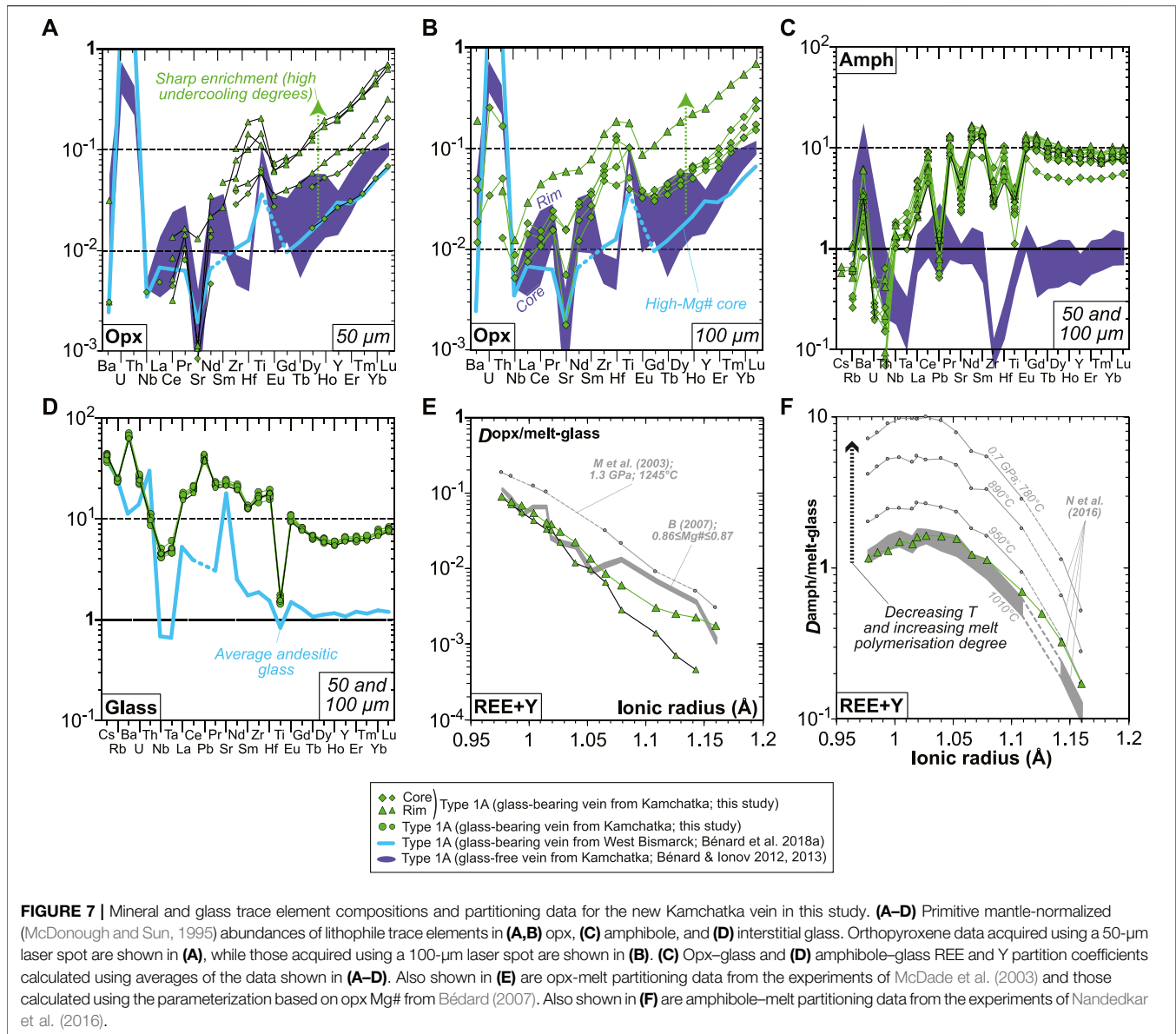
## Volatiles

Special attention was given in this study to volatile systematics between various glassy areas in the vein. Despite the frequent effect of micro-crystals on the Raman spectra of MIs (**Figure 8A**), deriving  $\text{H}_2\text{O}$  contents was possible using the OH vibration bands (**Figure 8B**). Water contents are variable in the interstitial glass ranging from virtually 0 (i.e., below the detection limit of  $\sim 0.05$  wt %) to  $\sim 2.5$  wt%, while higher abundances are generally found in the andesitic MIs (4–7 wt%; **Figure 8C**). Nearly all dacitic MIs appear to have lost much of their original  $\text{H}_2\text{O}$  endowments (mostly  $\leq 3.5$  wt%), but rare ones contain up to 7–10 wt%, suggesting a positive correlation of  $\text{H}_2\text{O}$  with  $\text{SiO}_2$  contents in undegassed inclusions (**Figure 8C** and **Supplementary Table S1**). F (100–400 ppm) and Cl (800–1,200 ppm) contents are consistent among interstitial glass and MIs (**Figure 8D** and **Supplementary Table S1**). The calculated amphibole–melt partition coefficients ( $D$ ) for these two volatile elements are relatively constant within the vein, with averages of  $1.1 \pm 0.3$  and  $0.11 \pm 0.01$  for F and Cl, respectively (**Figures 8E, F**).



S abundances display complex evolution trends that can be related to petrographic observations. S abundances are notably variable in each andesitic MI, where they may decrease from ~2,600 down to ~1,400 ppm toward vugs (Figure 9A and Supplementary Figure S10). Other vug-bearing andesitic MIs contain 800–1,000 ppm S, with the lowest S abundances analyzed in these inclusions ranging at ~400 ppm (Supplementary Figure S10 and Supplementary Table S1). Dacitic MIs generally contain  $\leq 400$  ppm S, some of which clearly include sulfide daughter crystals (Supplementary Figure S10 and

Supplementary Table S1). The interstitial glass displays lower S contents than the MIs ( $\leq 1,400$  ppm S), with notably more stable abundances next to vugs coated by sulfide alteration products such as Fe oxyhydroxide (400–600 ppm; Figure 9B). The presence of the latter secondary mineral as vug coatings appears to be widespread in the vein, as revealed by Fe mapping (Figure 9C and Supplementary Figure S9). Globally, S abundances decline from those within andesitic MIs to those in the interstitial glass at ~58 wt%  $\text{SiO}_2$ , ~4 wt%  $\text{FeO}$ , and 2–3 wt% MgO (Figures 9D–F).

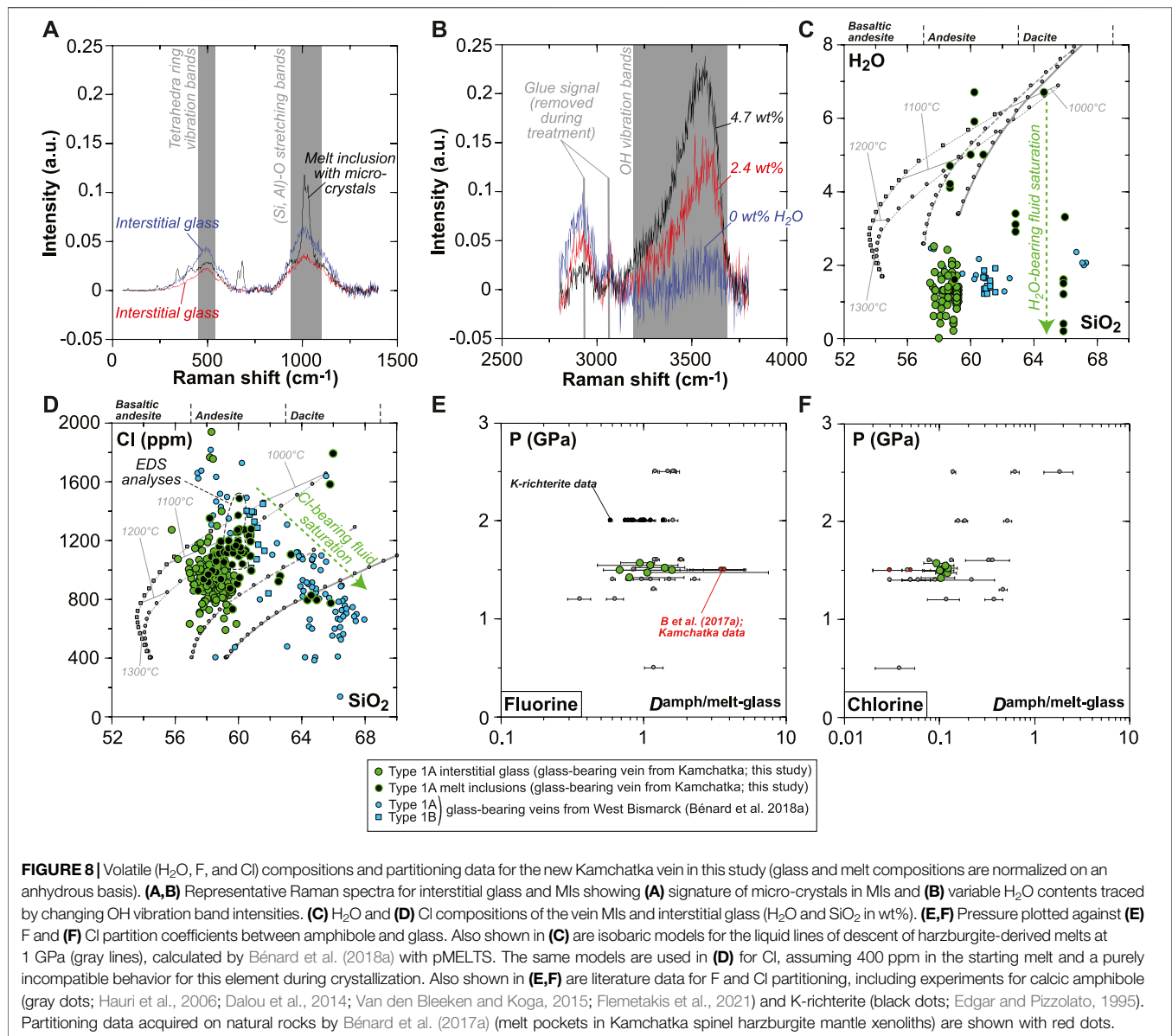


## DISCUSSION

### Undercooling and Differentiation of a Mantle-Derived Melt in the Sub-Arc Mantle Lithosphere

Several lines of evidence suggest that the orthopyroxenite vein from Kamchatka studied here formed by undercooling of a high-temperature, mantle-derived melt that intruded the sub-arc mantle lithosphere. The opx coarsening trend from the fringes to the vein center can be explained by the presence of a thermal gradient during the crystallization of the orthopyroxenite, with faster cooling rates at the fringes (Supplementary Figure S5). Normal zoning patterns in both major and trace elements in vein opx can also result from the

rapid crystallization of an undercooled silicate melt (Figures 3, 7, Supplementary Figure S6). If crystal growth is sufficiently fast to prevent anomalous lattice incorporation, boundary layers enriched in incompatible major elements form at melt–crystal interfaces (Watson, 1996; Watson and Müller, 2009). Such a process is indicated by zones of abrupt enrichment in Ti, Al, and sometimes Ca in vein opx (Figures 3, 7, Supplementary Figure S6). Similarly, the 10-fold increase in trace element concentrations in opx (e.g., REE and HFSE; Figure 7) appears difficult to reconcile with an equilibrium process, as this would require  $\geq 80\%$  crystallization. These observations are rather consistent with the extreme trace element enrichments of grain rims in some pegmatitic dykes, which result from kinetic disequilibrium during fast crystal growth driven by the intrusion of an



undercooled magma in a relatively cold country rock (e.g., London and Morgan, 2012).

A key textural feature in the orthopyroxenite vein in this study is the skeletal-hopper shape of some of the high-Mg# cores of opx (a typical tracer of fast cooling rates; e.g., Shea and Hammer, 2013), which contrasts with the generally euhedral borders outlining the low-Mg# rims of these elongated to blocky grains (Figure 3A). A sharp compositional interface is commonly observed between the high-Mg# cores and the low-Mg# rims of opx, which is consistent with the shapes of many major element profiles (Figure 3 and Supplementary Figure S6). These textural features are also coherent with the abrupt increases in Ti and Ca at Mg# ranging at 0.86–0.88 in the vein opx (Figures 4A,C and Supplementary Figure S4). In a first phase, major and trace elements were thus enriched in the silicate melt (i.e., disequilibrium growth with highest thermal gradient),

and in a second phase, opx rims formed from these enriched silicate melts. This two-phase undercooling regime can be explained in several ways, but the most likely process is that the original, high-temperature vein melt differentiated rapidly on cooling (first-phase growth of opx cores) to temperatures of the sub-arc mantle lithosphere (second-phase growth of opx rims). The association of skeletal-hopper cores with euhedral rims indicates that the first- and second-phase undercooling processes occurred in continuity, most likely because of decreasing cooling rates (Figure 3 and Supplementary Figure S6). More importantly, this provides favorable conditions for the attainment of equilibrium between the enriched grain rims and the last glass-forming residual melt.

The host harzburgite sample in direct contact with the orthopyroxenite vein in this study records equilibration temperatures of 897–932°C, as calculated using average olivine

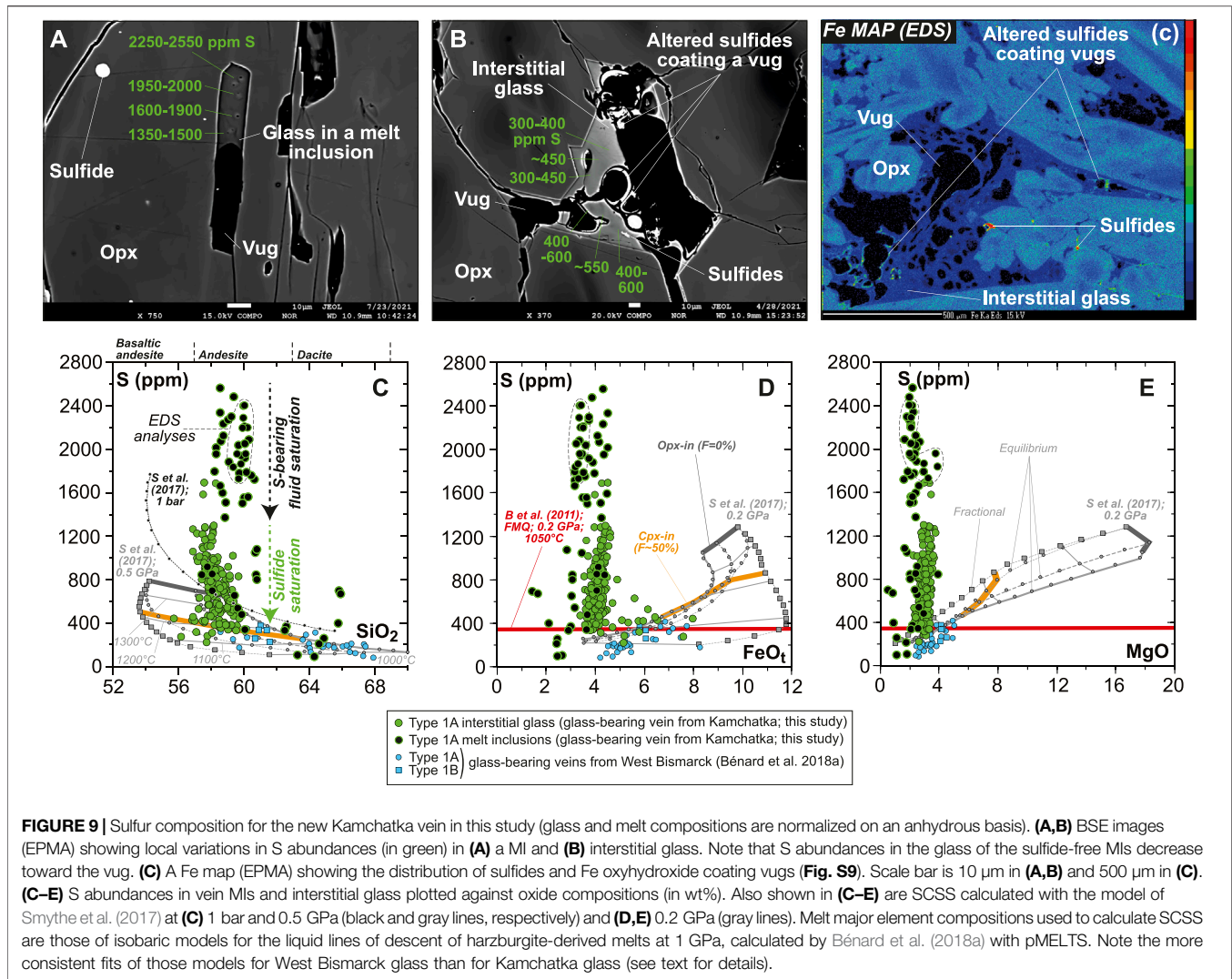


**FIGURE 9** | Sulfur composition for the new Kamchatka vein in this study (glass and melt compositions are normalized on an anhydrous basis). **(A,B)** BSE images (EPMA) showing local variations in S abundances (in green) in **(A)** a MI and **(B)** interstitial glass. Note that S abundances in the glass of the sulfide-free MIs decrease toward the vug. **(C)** A Fe map (EPMA) showing the distribution of sulfides and Fe oxyhydroxide coating vugs (**Fig. S9**). Scale bar is 10  $\mu\text{m}$  in **(A,B)** and 500  $\mu\text{m}$  in **(C)**. **(C-E)** S abundances in vein MIs and interstitial glass plotted against oxide compositions (in wt%). Also shown in **(C-E)** are SCSS calculated with the model of Smythe et al. (2017) at **(C)** 1 bar and 0.5 GPa (black and gray lines, respectively) and **(D,E)** 0.2 GPa (gray lines). Melt major element compositions used to calculate SCSS are those of isobaric models for the liquid lines of descent of harzburgite-derived melts at 1 GPa, calculated by Bénard et al. (2018a) with pMELTS. Note the more consistent fits of those models for West Bismarck glass than for Kamchatka glass (see text for details).

compositions and those of coarse and fine spinel grains (**Figure 2**) with the olivine-spinel geothermometer of O'Neill and Wall (1987) and Ballhaus et al. (1991) at 1 GPa. These pressure conditions match estimates for the crust–mantle transition in South Kamchatka (Bénard et al., 2018b). Similar values (898–918°C) are found using the opx–cpx thermobarometer of Brey and Köhler (1990), or a more recent equivalent with Equation 37 of Putirka (2008). They are also consistent with Ca-in-opx results using Brey and Köhler (1990) (923–941°C). All these estimates are in the range previously determined for Avacha spinel harzburgites (900–1,000°C; Ionov, 2010; Ionov et al., 2011; Bénard and Ionov, 2012, 2013; Bénard et al., 2016, 2017a, 2018c). Liquidus temperatures of the last residual melts in the orthopyroxenite vein can also be constrained using opx–glass thermometers, since some of the analyzed pairs appear to be both in Fe–Mg and trace element equilibrium (**Figures 6E, 7E**). Using Equations 28a, 28b of Putirka (2008), average temperatures of, respectively,  $1,118 \pm 8^\circ\text{C}$  and  $1,140 \pm 6^\circ\text{C}$  are calculated at 1 GPa, for a selection of opx rim–glass pairs recording  $K_D(\text{Fe-Mg}) > 0.2$  (all 1 $\sigma$ ; **Supplementary Table**

**S1**). In all these calculations,  $\text{H}_2\text{O}$  contents were set to the averaged measurements in the interstitial glass ( $1.2 \pm 0.5$  wt %); using  $5.1 \pm 0.9$  wt%  $\text{H}_2\text{O}$  as in the high-Mg# andesite MIs lowers these estimates by  $\sim 50^\circ\text{C}$  (all 1 $\sigma$ ; **Figure 8C**). From the previously mentioned temperature estimates, the undercooling degrees of the glass-forming, high-Mg# andesite melt range at ca. 100–200°C, depending on the extent of  $\text{H}_2\text{O}$ -rich fluid loss. Weak to inexistent core-to-rim zoning patterns in euhedral amphibole (crystallizing at  $\leq 1,100^\circ\text{C}$ ; e.g., Mandler and Grove, 2016) indicate that this mineral must have formed during this low-thermal gradient, second-phase undercooling process, as rims on opx.

The more primitive parental melt forming the strongly zoned opx grains must have been intruding the sub-arc mantle lithosphere at much higher temperatures than those estimated by opx–glass thermometry. According to experimental  $K_D(\text{Fe-Mg})^{\text{mineral-melt}}$ ,  $\text{Mg}\# \geq 0.91$  in the olivine and opx cores indicate crystallization from parental melts with  $\text{Mg}\# \geq 0.72$  (**Figures 2-4, Supplementary Figures S4, S6**; Beattie, 1993; Putirka, 2008; Waters and Lange, 2017). This

implies that the vein-forming melts originated from mantle peridotite sources. The formation of high-Mg# andesite, interstitial glass and MIs resulted from the quenching of residual liquids formed after the crystallization of abundant opx, minor olivine and spinel, and likely amphibole (Figure 6). Effects of the late-stage fractionation of amphibole is confirmed by the analysis of MIs, with direct textural evidence for daughter amphibole saturation and a Ca-depletion trend toward dacite compositions (Figure 6 and Supplementary Figure S9). Given the following observations: (i) high Cr# of spinel (Figure 2); (ii) low-Ti and alkali metals in the high-Mg# andesite, interstitial glass and MIs (Figures 6, 7, Supplementary Table S1); and (iii) low trace element levels in high-Mg# opx cores (e.g., HREEs; Figure 7), it can be deduced that the primitive parental melt of the orthopyroxenite vein was generated from refractory and depleted mantle sources (e.g., Klingenberg and Kushiro, 1996). Volatile analyses in the MIs show that they generally have higher H<sub>2</sub>O contents than in the interstitial glass but are otherwise similar in composition (except for S; Figures 8, 9). This suggests a damp melting process for the formation of the parental vein melts.

## A Parental Melt Formed From a Volatile-Poor Spinel Harzburgite Source

According to IUGS classification, (Ti, alkali metal)-depleted signatures of a high-Mg# andesite, such as is the case for the orthopyroxenite glass, indicate a boninitic affinity (Figures 6, 7, Supplementary Table S1; Le Bas, 2000). From the absence of cpx and the late-stage appearance of amphibole along the liquid line of descent, the results of experimental studies suggest that a spinel harzburgite mantle source can be envisaged for the vein-forming original melt (Umino and Kushiro, 1989; Klingenberg and Kushiro, 1996; Falloon and Danyushevsky, 2000; Parman and Grove, 2004).

The ability of an original melt to form low-Ti, high-Mg# andesite derivatives after a crystallization sequence dominated by opx can be further evaluated using the forward melt differentiation models in Bénard et al. (2018a). These authors used pMELTS software (Ghiorso et al., 2002) to model partial melting of spinel harzburgite sources at 1–1.5 GPa, 1,340–1,480°C,  $\Delta\log f_{O_2}[\text{FMQ}] = 0$ , and containing moderate, bulk H<sub>2</sub>O abundances (0.01–0.1 wt%). The results were found to be consistent with spinel harzburgite melting reactions from experimental studies (Parman and Grove, 2004), with modeled melting degrees (*F*) ranging mostly between 0.5 and 10%. The primary melts derived from spinel harzburgite melting models at 1,360°C were then used by Bénard et al. (2018a) to calculate the liquid lines of descent down to 1,000°C (opx + cpx ± olivine ± spinel fractionation) at 0.5–1 GPa. Here, we use the same models and further adapt them for discussing volatile evolution in the parental melts of orthopyroxenite veins (Figures 6, 8, 9).

The modeled liquid lines of descent at 1 GPa generally match closely the composition of the high-Mg# andesite glass in the orthopyroxenite vein. They differ in several

compositional parameters because the models predict cpx saturation at ~1,200°C for 0.01–0.05 wt% H<sub>2</sub>O in the source, and do not consider any amphibole solid solution model (Figure 6). Consequently, the vein glass appears too low in CaO (by ~2 wt%; Figure 6C) for a given degree of crystallization, most likely because of the effects of late-stage amphibole fractionation. However, ~2 wt% CaO induce only minor shifts in the other elements' contents during normalization, with ~1 wt% in SiO<sub>2</sub>, ~0.4 wt% in Al<sub>2</sub>O<sub>3</sub>, 0.01–0.08 wt% in FeO, MgO, Na<sub>2</sub>O, and K<sub>2</sub>O, and 0.001–0.007 wt% in TiO<sub>2</sub>, Cr<sub>2</sub>O<sub>3</sub>, MnO, NiO, and P<sub>2</sub>O<sub>5</sub>. Nevertheless, a consequence is that the comparison of CaO contents in the vein glass with those predicted by the models cannot be used to infer melt temperatures (Figure 6C). From the decreasing CaO with increasing SiO<sub>2</sub> contents in the vein glass; however, it can be deduced that the influence of amphibole fractionation seems to be crucial to form the rare high-Mg# dacite compositions identified for some of the vein MIs (Figure 6C). Overall, it appears that at least 50–60% crystallization of opx ± olivine ± spinel (cpx-in conditions; Figure 6B) is required to form the glass compositions found in the veins, when starting from an original melt derived from spinel harzburgite sources. These original melts can be designated as low-Ca or high-Si boninites, depending on the choice of classification (e.g., Crawford et al., 1989; Pearce and Reagan, 2019).

The pronounced zoning in lithophile trace elements in vein opx can hardly be reconciled with 50–60% crystallization, which we relate instead to boundary layer effects during fast crystal growth (Figure 7). A key physicochemical parameter of silicate melts controlling the production of such enrichment fronts is viscosity, which is inversely correlated with REE and HFSE diffusivities (e.g., Mungall, 2002 and references therein). Calculations by Bénard et al. (2018a) have shown that their modeled primary melts derived from spinel harzburgite originally have viscosities ranging between -0.2 and 0.7 log Pa·s, which are positively correlated with falling temperatures, as well as decreasing MgO and increasing H<sub>2</sub>O contents in the melts (i.e., lower melting degrees). In addition to the moderately to highly incompatible nature of REE and HFSE in opx (e.g., Bédard, 2007), further increase in melt viscosity throughout the liquid line of descent will be crucial to produce enrichment fronts in response to high undercooling degrees (Figure 6; Watson and Müller, 2009). It can be anticipated, therefore, that these enrichment processes will occur for any incompatible element or compound in opx, such as volatiles. As such, differentiation models can also be used, assuming a fluid-undersaturation state, to evaluate the volatile compositions of the original vein-forming melts and their spinel harzburgite sources. The analyses of H<sub>2</sub>O, F, Cl, and S in the MIs, in particular, provide reliable estimates of the maximum concentrations in melts which have suffered minimal volatile loss (Figures 8, 9).

The average H<sub>2</sub>O, F, and Cl contents in high-Mg# andesite MIs, which appear to be the least affected by saturation (H<sub>2</sub>O and Cl correlate with SiO<sub>2</sub>; Figure 8 and Supplementary Table S1) or devolatilization, are 5.1 ± 0.9 wt%, 260 ± 36 ppm, and 1,012 ±

62 ppm, respectively. The case of S is treated separately, since the formation of S-bearing fluids in many of the MIs appears to have altered the abundances of this element to much greater extents than for other volatiles (Figure 9 and Supplementary Figure S10). Assuming partial melting at 1 GPa and 1,360°C from a spinel harzburgite source, the crystallization degrees inferred from the differentiation models suggest that the original vein melt contained less than ca. 2–2.5 wt% H<sub>2</sub>O and ~400 ppm Cl (Figure 8). Note that all volatiles are considered here as purely incompatible, in line with the low partition coefficients for H<sub>2</sub>O and Cl in equilibrium experiments between Al-poor opx and melt (~10<sup>-3</sup>; Dobson et al., 1995; Hauri et al., 2006; Dalou et al., 2014; Bénard et al., 2017a; Urann et al., 2017). The volatile estimates for the original, vein-forming melts translate into 0.01–0.05 wt% H<sub>2</sub>O and ca. 2–8 ppm Cl in their spinel harzburgite sources (i.e.,  $F = 0.4$ –2% at 1 GPa and 1,360°C; Bénard et al., 2018a).

### Comparison With Earlier Studies of Kamchatka and West Bismarck Orthopyroxenite Veins and Some Alternative Processes for Their Formation

All the petrological and geochemical features implicating an original vein-forming melt derived from spinel harzburgite sources proposed here can also be found in the glass-free veins from Kamchatka (Bénard and Ionov, 2012, 2013) and the glass-bearing veins from West Bismarck (Bénard et al., 2018a). However, small differences do exist from one setting to another, which are either related to changes in the melt extraction rates from the conduit or in the thermobarometric conditions imposed when intruding the sub-arc mantle lithosphere.

The glass-free nature of the veins from Kamchatka in Bénard and Ionov (2012, 2013) indicates that the residual melts left after opx fractionation must have been efficiently expelled from the sampled conduit. This interpretation is consistent with the Mg# range of opx in the glass-free veins, which are typically limited to 0.89–0.92, while CaO contents can extend to elevated levels, as in the rims of the vein opx in this study (Figure 4). Because of high undercooling degrees, high-Mg# opx rapidly filled an open crack (hydraulic fracturing), and a high-Mg# andesite residual liquid, akin to that of the vein in this study, was expelled from the intergranular spaces in the sampled channel section. As such, the glass-free veins from Kamchatka can be interpreted as primitive crystal cumulates formed by parental melts derived from spinel harzburgite sources. This interpretation is also in line with the fact that the opx rims and the amphibole in these glass-free veins are less enriched in incompatible, lithophile trace elements than those in this study (Figure 7); mineral equilibration with a fractionating high-Mg# andesite melt residing in the conduit was more limited in the glass-free veins. In contrast, the F contents of amphibole in the glass-free veins are ca. 10–60 times higher than in this study (Figure 5), which could either result from variable F compositions of the spinel harzburgite sources and/or fluid-undersaturated conditions in the glass-free veins (see the following).

In both Kamchatka and West Bismarck, glass-bearing orthopyroxenites, the quenched phase is concentrated in the central part of the vein (Figure 7). This suggests that this

central part was relatively insulated (i.e., thermally and/or chemically) when compared with the fringes, which allowed the preservation of a residual melt after *in situ* differentiation. The West Bismarck interstitial glass ranges compositionally from high-Mg# andesite to dacite (Figure 6). The higher amounts of dacite glass in the West Bismarck setting can be explained by the lower equilibration temperatures of the sub-arc mantle lithosphere in this region than in Kamchatka (down to 650–700°C; Bénard et al., 2017b; Tollan et al., 2017; Bénard et al., 2018b). Mineral–glass equilibration temperatures in West Bismarck veins are similar to those in this study (1,114 ± 17°C), which indicates higher undercooling in the West Bismarck setting (≥300°C). The latter point is consistent with some of the specific textural features of West Bismarck veins, including skeletal and acicular shapes of pyroxenes or more frequent, oscillatory zoning patterns, which are expected at the highest undercooling degrees (L'Heureux and Fowler, 1996; Shea and Hammer, 2013). Other compositional differences exist between Kamchatka and West Bismarck vein glass, including higher lithophile trace element contents in this study (Figure 7). This appears to be mainly related to the absence of cpx formed from ~1,200°C along the liquid line of descent, since this phase tends to efficiently sequester some of the trace elements, such as HREEs, with temperatures decreasing below ~1,100°C (e.g., Wood and Blundy, 1997; Bénard et al., 2018a). Otherwise, the interstitial glasses in Kamchatka and West Bismarck veins are compositionally close, which includes the volatile contents left after fluid and sulfide saturation (Figures 8, 9).

Our inferences are at odds with earlier interpretations of Kamchatka glass-free orthopyroxenite veins as the direct products of the interaction of the sub-arc mantle lithosphere with a slab-derived liquid (reactions at 800–1,000°C with either a silicate melt or a fluid; Ishimaru et al., 2007; Ishimaru and Arai, 2008; Grant et al., 2016). In particular, the new combination of opx and glass data documents the high-temperature history of the veins, where melts derived from a refractory and depleted mantle intrude a relatively “cold” sub-arc lithosphere at >>1,100°C. Analyses of the first vein MIs further suggest a limited influence of a volatile-rich, slab-derived component in the spinel harzburgite sources. The inferred low H<sub>2</sub>O and Cl contents in such sources, in particular, do not exceed the typical budget of poorly metasomatized spinel harzburgite xenoliths from Kamchatka, which contain up to ~1 wt% amphibole (Ionov, 2010; Soustelle et al., 2010; Bénard et al., 2017a).

An alternative explanation of our findings could be related to the decompression melting of amphibole disseminated in the spinel harzburgite xenoliths during their transport to the surface (e.g., Bénard et al., 2021). At first glance, the SiO<sub>2</sub>-rich and high-Mg# nature of the liquids and minerals (opx and cpx; Bénard et al., 2021) produced during incongruent melting of amphibole could be compared to the orthopyroxenite vein assemblages. However, the low cpx and amphibole contents of the veins, together with the relatively CaO- and Cr<sub>2</sub>O<sub>3</sub>-poor compositions of their opx, are both inconsistent with an amphibole melting process (Supplementary Figure S11). Instead, these compositions require the dominant contribution of opx melting in spinel harzburgite sources to produce the MgO-

rich vein original melts. This preferred interpretation is further substantiated by sulfide analyses, which are provided in the second article of this two-part study.

## Lithophile Trace Element and Volatile Partition Coefficients

Equilibrium exchange and partition coefficients calculated using grain rims in this study are generally consistent with literature data (Figures 6–8). A deviation from experimental results is, however, the  $K_D(\text{Fe-Mg})^{\text{amphibole-melt}}$ , which appears lower in the orthopyroxenite vein than in literature datasets for andesite to rhyolite melts (Figure 6E; Klein et al., 1997; Nandedkar et al., 2016). Since  $\text{H}_2\text{O}$  contents measured in the experiments of Nandedkar et al. (2016) (9–13 wt%) are much higher than in the vein interstitial glass (~1 wt%), it is possible that the deviation in  $K_D(\text{Fe-Mg})^{\text{amphibole-melt}}$  results from the effects of variable volatile contents in the melt phase. A positive relationship between  $\text{H}_2\text{O}$  contents and  $K_D(\text{Fe-Mg})$  has notably been found in opx-melt equilibration experiments (Waters and Lange, 2017).

In the case of lithophile trace elements, good fits are observed between the orthopyroxenite vein data and those in Bédard (2007) and Nandedkar et al. (2016), respectively, for opx-melt and amphibole-melt experiments (Figures 7E,F). This suggests that kinetic disequilibrium during the second-phase undercooling process of the glass-forming, high-Mg# andesite melt played a minor role. However, the second-phase cooling rate was insufficiently slow for the most incompatible trace elements (e.g., LREEs and LILE in amphibole; Figure 7F and Supplementary Table S1) to attain equilibrium partitioning. The temperature effect on the amphibole-melt partition coefficients is prominent, which has been interpreted as imposed by the structure of the silicate melt (increasing polymerization degree; Figure 7F; Nandedkar et al., 2016). A comparison of the latter experiments with those of Brenan et al. (1995) and Klein et al. (1997) suggests that this temperature effect is considerably more pronounced than the influence of pressure on a 0.7–1.5 GPa range, which allows the use of amphibole-melt partition coefficient as a geothermometer. A temperature of ~1,000°C is the most appropriate for the formation of euhedral amphibole in the orthopyroxenite vein (Figure 7F). This indicates that the formation of hydrothermal fluids from the high-Mg# andesite, residual melt in the vein also occurred at relatively high temperatures; vapor saturation from a similar silicate melt was also inferred to proceed at 950–1,010°C in the experiments of Nandedkar et al. (2016) at 0.7 GPa.

The partition coefficients for F and Cl between amphibole and melt generally agree with experimental data for calcic amphibole and K-richrichterite (Edgar and Pizzolato, 1995; Hauri et al., 2006; Dalou et al., 2014; Van den Bleeken and Koga, 2015; Flemetakis et al., 2021). The general tendency of F being compatible (or slightly incompatible) and Cl being incompatible in amphibole is thus confirmed (Van den Bleeken and Koga, 2015; Bénard et al., 2017a). This tendency is notably more pronounced for calcic amphibole equilibrated with low- $\text{H}_2\text{O}$  andesite (~0.2 wt%) in sub-arc mantle peridotites reported by Bénard et al. (2017a), where F was found to be compatible (partition coefficients up to

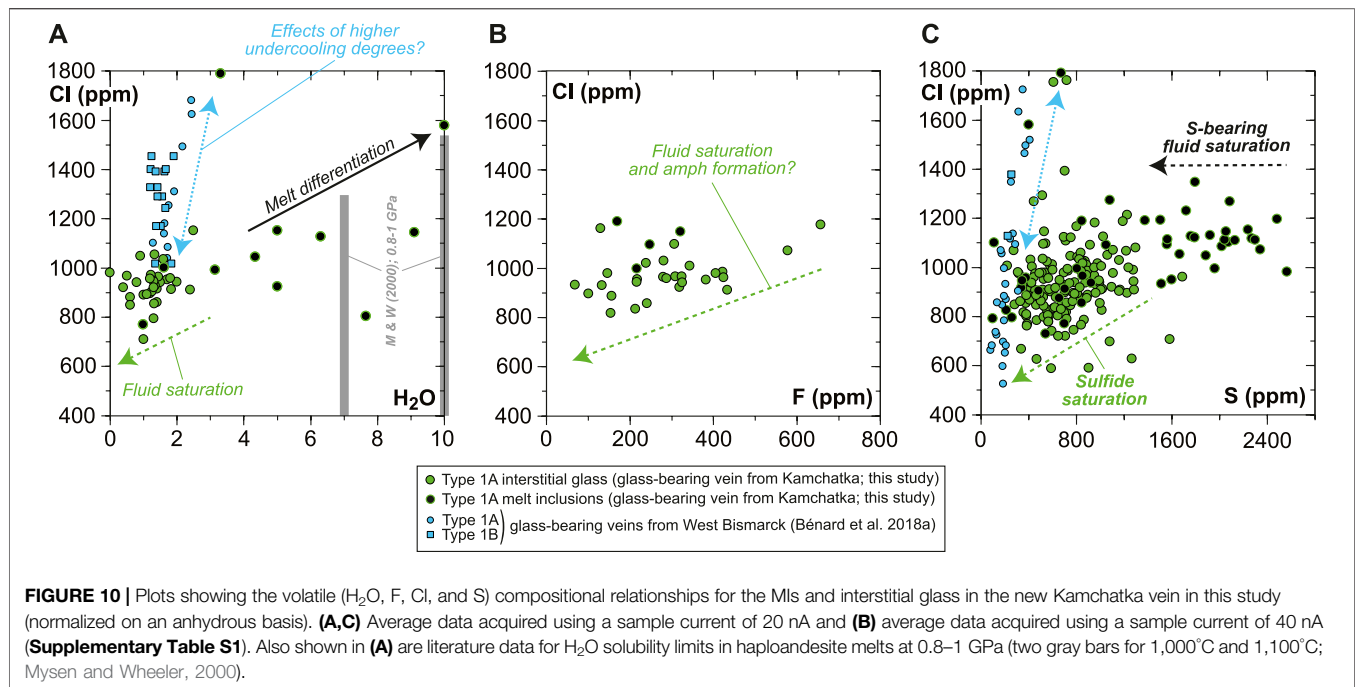
~3.6) and Cl highly incompatible in amphibole (partition coefficients down to 0.03–0.05). Both the Al/(Si + Al) and  $\text{H}_2\text{O}$  contents of the silicate melt have already been demonstrated to affect F and Cl solubility in contrasting ways (Dalou et al., 2015; Dalou and Mysen, 2015), notably resulting in a decrease in F partition coefficients and an increase in those of Cl for pyroxenes in more hydrous compositions (Dalou et al., 2014). Assuming similar pressure and temperature (P–T) conditions, and given the close Al/(Si + Al) in all the investigated andesite glass, an effect of  $\text{H}_2\text{O}$  on amphibole-melt partitioning would also explain the slight differences between the measurements in this study and those in Bénard et al. (2017a). Further experimental investigations are required, however, to confirm that such a mechanism exists for the partitioning of halogens between amphibole and melt.

## Fluid Saturation and Hydrothermal Sulfide Formation in Melts Derived From Spinel Harzburgite Sources

The loss of volatiles from the residual melt to a hydrothermal fluid phase is evidenced by the presence of curvilinear vugs (former bubbles) and decreases in  $\text{H}_2\text{O}$ , F, Cl, and S concentrations in the glass of both Kamchatka and West Bismarck veins (Figures 1, 3, 5, 8–10, Supplementary Figures S3, S5–S10; Bénard et al., 2018a). Saturation in a hydrothermal phase likely started *in situ* (i.e., during isobaric cooling upon melt emplacement) and from temperatures at least as high as ~1,000°C since amphibole F and Cl compositions reflect fluid-saturated conditions (Figures 5, 7). The halogen-rich nature of the hydrothermal fluids is further indicated by the presence of Cl-rich amphibole (5,000–6,000 ppm; Supplementary Table S1) growing from the border of the vugs toward their cores (i.e., heterogeneous nucleation of a hydrothermal mineral; Supplementary Figure S9). In the West Bismarck case, these vugs are frequently accompanied by sulfide-rich vesicles (Bénard et al., 2018a).

The  $\text{H}_2\text{O}$  solubility limits of haploandesite melts at 0.8–1 GPa range from 6–9 wt% at 1,100°C to 7–10 wt% at 1,000°C (Mysen and Wheeler, 2000), which are very close to the uppermost abundance levels of the vein MIs (up to 6–7 wt%  $\text{H}_2\text{O}$  in high-Mg# andesite and up to 7–10 wt%  $\text{H}_2\text{O}$  in high-Mg# dacite; Figure 10A and Supplementary Table S1). However, most of the high-Mg# andesite MIs show a weak positive correlation between  $\text{H}_2\text{O}$ , Cl, and  $\text{SiO}_2$  contents and contain lower  $\text{H}_2\text{O}$  concentrations on average ( $5.1 \pm 0.9$  wt%; Figures 8, 10A). This suggests that the original melts were  $\text{H}_2\text{O}$ -undersaturated. It appears, therefore, that crystallization led to isobaric fluid saturation in some of the residual melts formed in the vein at sub-arc mantle depths. Shortly after saturation, devolatilization must have occurred during the ascent of the xenoliths and the vein-trapped, undercooled melts to the surface. This is suggested by the final, low  $\text{H}_2\text{O}$  contents in the interstitial glass (Figures 8, 10A), consistent with the strong positive relationship between pressure and  $\text{H}_2\text{O}$  solubility in haploandesite melt (Mysen and Wheeler, 2000).

In contrast with  $\text{H}_2\text{O}$  concentrations, the abundances of Cl in both the interstitial glass and MIs are far below the solubility



limits of this element in hydrous andesite at high pressure (e.g., Webster et al., 1999). However, Cl abundances decrease progressively with increasing  $\text{SiO}_2$  contents of the interstitial glass, from the onset of  $\text{H}_2\text{O}$ -rich fluid saturation in high-Mg# andesite attaining  $\sim 7$  wt%  $\text{H}_2\text{O}$  (Figure 8). This progressive trend is at odds, for instance, with the sharp decline in S concentrations (Figure 9), and most likely reflects a structural control on Cl solubility at saturation in a  $\text{H}_2\text{O}$ -rich fluid (e.g., decreasing (Al + Na + Ca + Mg)/Si of the silicate melt; Webster, 1997a, 1997b; Webster et al., 1999). The F budget might have been affected by fluid exsolution as well, since F is poorly correlated with Cl in the interstitial glass (Figure 10B and Supplementary Table S1). However, the extent of this process is uncertain for the case of F. The near-compatible nature of F in amphibole might have also contributed to the observed correlation with Cl.

Variable S abundances characterize some of the sulfide-free MIs, with a typical decrease from  $\sim 2,600$  ppm to  $\sim 1,400$  ppm toward vugs (formerly bubbles), corresponding to the upper abundances in the interstitial glass (Figures 9, 10C, Supplementary Figure S10). The drop of S in MIs likely results from the efficient partitioning of S from the low- $\text{FeO}_t$  andesite melt into a ( $\text{H}_2\text{O}$ , Cl)-rich hydrothermal phase at fluid saturation (e.g., Zajacz et al., 2012). Diffusion of some of the major elements, such as Fe (Zajacz et al., 2012; Venugopal et al., 2020), from the melt into the hydrothermal phase can also occur at high temperatures, which must have led to the formation of vug-hosted sulfides in some of the MIs and low S contents in their glass (Figure 9 and Supplementary Figure S10). If sulfide globules of clear magmatic origin can be found as inclusions in vein opx, or in the coexisting, interstitial glass (Figures 1, 9, Supplementary Figures S3, S5–S10; Bénard et al., 2018a), hydrothermal sulfides must have also

resided at the edges of many fluid-derived vugs, where they are now found as Fe oxyhydroxide coatings (Figure 9 and Supplementary Figure S9). Oxyhydration of sulfides to form goethite, for instance, is common when deuteric alteration occurs (e.g., Lorand, 1990). The formation of hydrothermal sulfides is also consistent with the presence of sulfide-rich vesicles in the interstitial glass of the West Bismarck veins (Supplementary Table S1; Bénard et al., 2018a). The most likely explanation is, therefore, that these widespread hydrothermal sulfides were produced in a process of S solubilization from the vein parental melts into high-temperature fluids (Figure 9), shortly after or concurrently with the onset of magmatic sulfide formation (i.e., from  $\sim 1,100^\circ\text{C}$  at  $\sim 1$  GPa; Zhang and Hirschmann, 2016).

## Redox-Induced Formation of Magmatic Sulfides in Melts Derived From Spinel Harzburgite Sources

While MI data trace the role of a ( $\text{H}_2\text{O}$ , Cl)-rich, S-bearing fluid in the formation of hydrothermal sulfides, further evolution of S abundances from  $\sim 1,400$  ppm down to 200–300 ppm in the interstitial glass and some MIs may be related to the precipitation of abundant magmatic sulfides from  $\sim 1,100^\circ\text{C}$  down to  $\leq 850^\circ\text{C}$  (Figure 9; Craig and Kullerud, 1969; Kullerud et al., 1969; Fleet et al., 1993; Fleet and Pan, 1994; Zhang and Hirschmann, 2016). Calculations of the sulfur content at sulfide/sulfate saturation (SCSS) with the recent parameterization of Smythe et al. (2017), considering the major element compositions from the differentiation models of Bénard et al. (2018a), show that 200–300 ppm can be expected in a high-Mg# andesite melt at sulfide saturation,

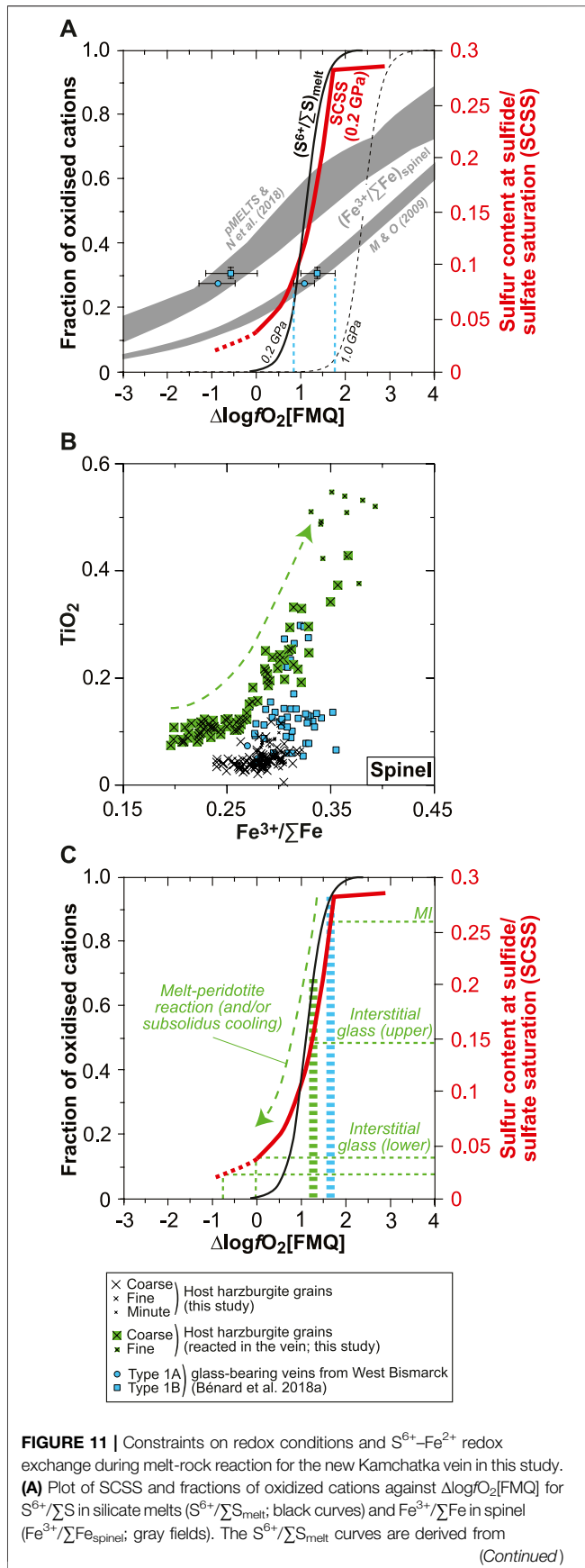


**FIGURE 11 |** experiments at 0.2 GPa (solid curve; Jugo et al., 2010; Klimm et al., 2012) and 1.0 GPa (dashed curve; Matjuschkin et al., 2016). The  $Fe^{3+}/\Sigma Fe_{spinel}$  values were calculated by Bénard et al. (2018a) using experimental  $Fe^{3+}$  and  $Fe^{2+}$  partition coefficients from Mallmann and O'Neill (2009), and pMELTS and SPINMELT-2.0 (Nikolaev et al., 2018). In both cases,  $Fe^{3+}/\Sigma Fe_{melt}$  was estimated with the model of Kress and Carmichael (1991), using the melt major element compositions calculated with pMELTS for spinel harzburgite melting at 1 GPa, 1,360°C, and with 0.01 wt% and 0.05 wt%  $H_2O$  (Bénard et al., 2018a). Also shown are experimental SCSS values for an andesite melt at 0.2 GPa (red curve; Botcharnikov et al., 2011). These data are compared with the calculated  $Fe^{3+}/\Sigma Fe_{spinel}$  for magmatic grains in West Bismarck orthopyroxenite veins and the corresponding theoretical  $fO_2$  conditions (blue symbols and dashed lines; **Figures 2C–F**; Bénard et al., 2018a). See text for details. **(B)** Plot of  $TiO_2$  contents (in wt%) against calculated  $Fe^{3+}/\Sigma Fe$  in spinel. **(C)** Same plot as in **(A)** but showing representative S abundances measured in the MIs and interstitial glass of the new Kamchatka vein in this study and the corresponding, theoretical  $fO_2$  conditions (dashed green lines). Also shown are  $fO_2$  conditions inferred from magmatic spinel grains in West Bismarck orthopyroxenite veins (dashed blue bar; Bénard et al., 2018a) and from the host spinel harzburgite in this study (dashed green bar; see text for details).

0.2–0.5 GPa and 1,000–1,100°C (**Figure 9**). These values are consistent with the high-pressure experimental results of Botcharnikov et al. (2011), but only for redox conditions in a range of  $-1 \leq \Delta\log fO_2$ [FMQ]  $\leq 0$  (**Figures 9, 11A**). However, elevated S contents in the volatile-rich vein MIs in this study (1,400–2,600 ppm; **Figure 9**) are at odds with the predictions from  $S^{2-}$  capacity models for a high-Mg# andesite melt equilibrated at  $\Delta\log fO_2$ [FMQ]  $\leq 0$  (e.g., up to ~1,400 ppm at 1 bar and 1,400°C in the Cape Vogel andesite; O'Neill and Mavrogenes, 2002). The new observations in this study, therefore, can only be reconciled if  $fO_2$  variations occurred during the formation of the orthopyroxenite veins.

It is well known that the S solubility in silicate melts of various compositions is positively correlated with  $fO_2$ , as a result of the  $S^{2-}$  to  $S^{6+}$  transition (e.g., Jugo et al., 2010; Botcharnikov et al., 2011; Klimm et al., 2012). In andesite melts, SCSS increases sharply from ~250 to ~2,750 ppm at 0.2 GPa, 1,050°C, and for  $\Delta\log fO_2$  [FMQ] ranging from  $-1$  to  $+2$  (**Figure 11A**; Botcharnikov et al., 2011). Even though the relationships between SCSS or  $(S^{6+}/\Sigma S)_{melt}$  (where  $\Sigma S = S^{2-} + S^{6+}$ ) and  $fO_2$  could be modified at higher pressure conditions (**Figure 11A**; Mavrogenes and O'Neill, 1999; Moretti and Baker, 2008; Matjuschkin et al., 2016), these solubility values roughly correspond to the range of S abundances measured in the vein glasses in this study and in Bénard et al. (2018a) (**Figure 9**). On top of the constraints from SCSS, EPMA analyses of spinel in West Bismarck veins are sufficiently precise to derive their  $Fe^{3+}/\Sigma Fe$  (where  $\Sigma Fe = Fe^{2+} + Fe^{3+}$ ) by stoichiometric calculations. In the light of the contrasting origin of spinel in the orthopyroxenite veins outlined in this study (as shown later), we select the  $(Fe^{3+}/\Sigma Fe)_{spinel}$  from grains of demonstrated magmatic origin (i.e.,  $Cr \geq 0.75$ ; **Figure 2**) in the West Bismarck database to plot them in **Figure 11A**. Different  $Fe^{3+}$ - $Fe^{2+}$  distribution models between spinel and melt provide contrasting results, using either thermodynamic modeling (Ghiorso et al., 2002; Nikolaev et al., 2018) or experimental partitioning coefficients (Mallmann and O'Neill, 2009). However, the second approach

was already compared successfully with oxybarometry calculations (Bénard et al., 2018c) and provides an estimate of  $+1 \leq \Delta \log f_{\text{O}_2}[\text{FMQ}] \leq +1.5$  from the vein  $\text{Fe}^{3+}/\sum \text{Fe}_{\text{spinel}}$  (Figure 11A). Both SCSS and  $\text{Fe}^{3+}/\sum \text{Fe}_{\text{spinel}}$  data, therefore, suggest that the orthopyroxenite parental melts were originally equilibrated at  $\Delta \log f_{\text{O}_2}[\text{FMQ}] \sim +1.5$  (Figure 11A).

There are several pieces of evidence for the involvement of a melt-rock reaction process during the emplacement of the vein parental melts in this study. These notably include profiles in the neighboring host harzburgite olivine or the presence of olivine and spinel relics from the host directly inside the vein (Figures 2, 5, Supplementary Figures S3, S7). In the case of spinel relics, amphibole formation from these grains suggests that they have been partially consumed and re-equilibrated with the percolating melt through a peritectic reaction, as traced by grain-scale profiles and the continuous evolution of their compositions from the host harzburgite to within the vein (Figure 2 and Supplementary Figure S7). Using stoichiometric calculations for the whole spinel relic dataset, it emerges that this melt-rock reaction process is also reflected in their  $\text{Fe}^{3+}/\sum \text{Fe}$ , with a positive correlation between this parameter from  $\sim 0.25$  to  $\sim 0.35$  and  $\text{TiO}_2$  contents (Figure 11B). The oxidizing effect of the percolating melt can be even traced in the neighboring host harzburgite, which records  $+1 \leq \Delta \log f_{\text{O}_2}[\text{FMQ}] \leq +1.2$  calculated with the oxybarometers of Wood et al. (1990) and Ballhaus et al. (1991) at 1 GPa and using the olivine–spinel equilibration temperatures (Figure 11C). The abundant, fine-grained spinel formed in the host harzburgite opx pseudomorphs can be further interpreted as a petrographic signature of this oxidation process (Supplementary Figure S2).

Taken collectively, the observations and calculations mentioned before can be reconciled in a model where the vein parental melts were originally oxidized at  $\Delta \log f_{\text{O}_2}[\text{FMQ}] \sim +1.5$  and contained  $\sim 2,600$  ppm of S, mostly dissolved as  $\text{S}^{6+}$  (MI data; Figure 11C). The whole range in S abundances in the vein glasses, therefore, not only records the formation of hydrothermal fluids but also a melt-rock reaction process where  $\text{S}^{6+}$  was locally reduced to  $\text{S}^{2-}$  through a redox reaction with  $\text{Fe}^{2+}$ -bearing mantle minerals (interstitial glass data; Figure 11C). This suggests that the original vein melt was undersaturated in  $\text{H}_2\text{O}$ , F, Cl, and sulfide when intruding the sub-arc mantle. Given that sulfide starts crystallizing from  $\sim 1,100^\circ\text{C}$  at  $\sim 1$  GPa (e.g., Zhang and Hirschmann, 2016), saturation of the silicate melt with a sulfide liquid is the volatile exsolution process that occurred at the highest temperatures in the veins at sub-arc mantle depths (formation of a Fe-Ni-Cu-S-O “matte” precursor to sulfide minerals; e.g., Fonseca et al., 2008). The presence of some magmatic sulfide globules found as inclusions in high-Mg# opx cores indeed suggests that saturation in a sulfide liquid occurred during the first-phase undercooling process (Figures 1, 9, Supplementary Figures S3, S5–S10). This means that redox reactions with the host harzburgite were initiated just upon the intrusion of the original melt in the sub-arc mantle.

The combination of  $\text{S}^{6+}$ – $\text{Fe}^{2+}$  redox exchange during melt-rock reaction and S capture in ( $\text{H}_2\text{O}$ , Cl)-rich hydrothermal fluids is key to trigger the formation of abundant sulfides in melts derived from spinel harzburgite sources. During such a

process at  $\geq 0.2$  GPa, up to 85% of the original S content in melts is locally precipitated as magmatic and hydrothermal sulfides (Figure 9). This appears to be primarily facilitated by the relatively low  $\text{FeO}_t$  contents of the derived high-Mg# andesite melts, which lower SCSS and favor the partitioning of  $\text{S}^{2-}$  into hydrothermal fluids (e.g., Zajacz et al., 2012; Smythe et al., 2017).

## CONCLUSIONS

We report a detailed petrological and geochemical study of a sulfide- and glass-bearing orthopyroxenite vein transecting a mantle-derived spinel harzburgite xenolith from the Kamchatka arc. The primary conclusions of this study are as follows:

- i) The glass formed by quenching of residual liquids left after the crystallization of abundant opx (strongly zoned enstatite), amphibole (magnesio-hornblende), and minor olivine (forsterite) and spinel (chromite). The interstitial glass has a low-Ti ( $\leq 0.4$  wt%  $\text{TiO}_2$ ) and high-Mg# (0.4–0.6) andesite composition.
- ii) The interstitial glass has a wide range of  $\text{H}_2\text{O}$  (0–2 wt%) and S (200–1,400 ppm) contents, whereas F (100–400 ppm) and Cl (800–1,200 ppm) are generally less variable, as in coexisting amphibole (200–400 ppm F and 100–150 ppm Cl). Trace element partition coefficients, including those for halogens between amphibole and melt, are calculated using the compositions of interstitial glass and coexisting minerals. Despite having a similar andesitic composition, most of the opx-hosted melt inclusions contain much more  $\text{H}_2\text{O}$  (4–7 wt%) and S (up to  $\sim 2,600$  ppm) than the interstitial glass.
- iii) As previously deduced for glass-free veins from Kamchatka and glass-bearing veins from the West Bismarck arc, the orthopyroxenite in this study formed by cooling of parental melts (low-Ca boninite; LCB), which were originally produced by low-degree ( $\leq 5\%$ ), second-stage melting of spinel harzburgite at  $\geq 1,360^\circ\text{C}$  and  $\leq 1.5$  GPa. Using the new volatile data, we further infer that this harzburgite source cannot have contained significantly more than 0.01–0.05 wt%  $\text{H}_2\text{O}$  and a few ppm of halogens.
- iv) Petrological and sulfur solubility models, thermo-barometric calculations, and partitioning data indicate that the original vein-forming LCB melt intruded the sub-arc mantle lithosphere at  $\geq 1,300^\circ\text{C}$ , where it partially crystallized (50–60%; opx + amphibole  $\pm$  olivine  $\pm$  spinel fractionation) to form high-Mg# andesitic derivative liquids at ca. 1,050–1,100°C. The original vein-forming melt was relatively oxidized, recording oxygen fugacity conditions  $\sim 1.5$  log units above the fayalite–magnetite–quartz oxygen buffer.
- v) Redox exchange between  $\text{S}^{6+}$  in the original melt and  $\text{Fe}^{2+}$  in the host mantle minerals, together with saturation in a S-bearing, ( $\text{H}_2\text{O}$ , Cl)-rich hydrothermal fluid during cooling, concurrently led to the formation of abundant

sulfides in the orthopyroxenite. During this process, up to 85% of the original melt S content (~2,600 ppm) was locally precipitated as magmatic and hydrothermal sulfides. As such, melts derived from spinel harzburgite sources can concentrate chalcophile and highly siderophile metals in orthopyroxenite dykes and sills.

## DATA AVAILABILITY STATEMENT

The original contributions presented in the study are included in the article/**Supplementary Material**, further inquiries can be directed to the corresponding author.

## AUTHOR CONTRIBUTIONS

AB acquired and treated the whole dataset in this study, except for Raman micro-spectroscopic data, which were acquired and treated by CL. AB wrote the manuscript with later contributions from all the co-authors.

## FUNDING

This work was supported by the Australian Research Council (DE120100513 to ON and DP120104240 to RA and ON) at ANU. AB received funding from the European Union's Horizon 2020 research and innovation program under the Marie Skłodowska-Curie grant agreement 844795 at UNIL. CL received support from a Chaire d'Excellence IDEX19C627X/FD070/D110 from the ANR IdEX Université de Paris 18-IDEX-0001. R Rapp and JW Park provided assistance, respectively, with EPMA and LA-ICPMS analyses at ANU. C De Meyer and A Demers-Roberge provided assistance with SEM analyses at UNIL.

## SUPPLEMENTARY MATERIAL

The Supplementary Material for this article can be found online at: <https://www.frontiersin.org/articles/10.3389/feart.2022.867979/full#supplementary-material>

**Supplementary Figure S1** | Chart records of counts on F (dark gray) and Cl (gray) peaks against time for glass halogen analyses (EPMA) using a focused beam and a defocused beam of 20  $\mu\text{m}$  (indicated in the bottom left corner). Note that none of these beam conditions lead to a decrease of either F or Cl counts with time, while count variability is reduced when using a defocused beam.

**Supplementary Figure S2** | Photomicrograph in transmitted light of the new Kamchatka sample in this study and BSE images (EPMA), showing textural features of the spinel harzburgite part (host) of this composite sample. Top: coarse- and fine-grained spinel and coarse-grained olivine; scale bar is 100  $\mu\text{m}$ . Middle: cpx- and amphibole-bearing, fine-grained opx pseudomorphs; scale bar is 100  $\mu\text{m}$ . Bottom: minute spinel inclusions in fine-grained opx pseudomorphs; all scale bars are 100  $\mu\text{m}$ , except for BSE image insets, which are 1 or 10  $\mu\text{m}$ . Note the absence of glass in the host spinel harzburgite.

**Supplementary Figure S3** | Olivine major element compositions (in wt% for oxides) analyzed in different parts of the new Kamchatka sample in this study. Top: major element maps (EPMA) of the Type 1A vein rim; elements mapped are indicated in the

top left corner and scale bar is 500  $\mu\text{m}$ . Top middle: photomicrograph in transmitted light, BSE images (EPMA), and profiles for olivine from the spinel harzburgite part (host); scale bar is 100  $\mu\text{m}$ . Bottom middle: BSE images (EPMA) and profiles for olivine against the Type 1A vein rim; scale bar is 100  $\mu\text{m}$ . Bottom: BSE images (EPMA) and profiles for olivine from a host spinel harzburgite fragment in the Type 1A vein; scale bars are all 100  $\mu\text{m}$ , except for BSE image insets, which are 10 or 100  $\mu\text{m}$ . Note the limited amount of glass in the vein rims, contrasting with the presence of abundant sulfides.

**Supplementary Figure S4** | Pyroxene major element compositions (in wt% for oxides) analyzed in different parts of the new Kamchatka sample in this study. Top: photomicrograph in transmitted light, BSE images (EPMA), and profiles for fine-grained opx pseudomorphs from the spinel harzburgite part (host); scale bar is 100  $\mu\text{m}$ . Middle: opx major element compositions, including a comparison of the Type 1A vein and host spinel harzburgite parts of the new sample with literature data. Bottom: cpx major element compositions, including a comparison of the host spinel harzburgite part of the new sample with literature data.

**Supplementary Figure S5** | Photomicrograph in transmitted light and BSE images (EPMA) showing the rim (left) and central part (right) textural features of the Type 1A vein cutting the new Kamchatka sample in this study. Scale bar is 100  $\mu\text{m}$ . Note that opx grain size and glass abundance increase from the rim to the central part of the vein.

**Supplementary Figure S6** | BSE images (EPMA) and rim-to-rim profiles (in wt% for oxides) for opx grains from the Type 1A vein cutting the new Kamchatka sample in this study. All scale bars are 100  $\mu\text{m}$ , except for profile Z8\_1, which is 10  $\mu\text{m}$ . Note that opx core composition can evolve from primitive ( $\text{Mg}\# > 0.9$ ) to slightly more evolved ( $\text{Mg}\# < 0.9$ ), in concert with other elements, while  $\text{Cr}_2\text{O}_3$  reverse zoning sometimes occurs in the most primitive grains.

**Supplementary Figure S7** | BSE images, major element maps (all acquired using EPMA), and profiles (in wt% for oxides) for anhedral (i.e., replacing coarse spinel from the host harzburgite) amphibole grains from the new Kamchatka vein in this study. Top: BSE images with variable contrast; scale bar is 100  $\mu\text{m}$ . Middle: major element maps; elements mapped are indicated in the top left corner and scale bar is 500  $\mu\text{m}$ . Bottom middle: BSE images and profiles; scale bar is 100  $\mu\text{m}$ . Note variations in  $\text{Mg}\#$ ,  $\text{Cr}\#$ , and  $\text{MnO}$  and  $\text{NiO}$  contents in reacted spinel relics (originally coarse grains from the host harzburgite), which are traced by the combination of major element maps and profiles.

**Supplementary Figure S8** | BSE images (EPMA) and profiles (in wt% for oxides) for euhedral amphibole grains from the new Kamchatka vein in this study. Scale bar is 100  $\mu\text{m}$ . Note the small variations in  $\text{Cr}\#$  in euhedral amphibole grains when compared with the anhedral ones (i.e., replacing coarse spinel from the host harzburgite; dashed lines), while sometimes  $\text{Mg}\#$  slightly decreases from core-to-rim in the former type.

**Supplementary Figure S9** | BSE images (SEM) and related, representative EDS spectra for the new Kamchatka vein in this study. Top: chromite inclusions in vein opx. Orange peaks in the related EDS spectra (yellow) are fits to the V and Zn Ka and Kb emission lines. Second from top: sulfide alteration products coating a vug in interstitial glass (Figure 9b), which also contains a cluster of sulfide micro-grains. Using EDS analysis, this alteration material is identified as Fe oxyhydroxide. Third from top: cluster of sulfide micro-grains shown above, which is partially located beneath the surface of the interstitial glass. Note the slight S KaKb peak in the related EDS spectra. Fourth from top: a sulfide globule included in vein opx, which has been entirely altered into Fe oxyhydroxide. Fifth from top: a MI included in vein opx and containing daughter micro-crystals. As seen in the related EDS spectra, a slight increase in the Ca Ka peak's intensity occurs when moving the beam from the MI's glass to its daughter crystals, allowing these latter to be identified as amphibole. Bottom: a vug in interstitial glass containing not only the common altered sulfide coating but also amphibole micro-crystals at its edges. As seen in the related EDS spectrum, a clear bump is related to the Cl Ka peak, whereas this is not the case for the F Ka peak, which is overlapped by the Fe L emission lines.

**Supplementary Figure S10** | BSE images (EPMA) showing local variations in S abundances (in green) in MIs from the new Kamchatka vein in this study, some of which contain sulfides. Note that, as shown in Figure 9, S abundances in the glass of sulfide-free MIs frequently decrease toward vugs.

**Supplementary Figure S11** | Pyroxene major element compositions (in wt% for oxides) for the new Kamchatka sample in this study, compared with data for amphibole incongruent melting relics and products in spinel harzburgite matrix (yellow dots; Bénard et al. 2021).

## REFERENCES

- Ballhaus, C., Berry, R. F., and Green, D. H. (1991). High Pressure Experimental Calibration of the Olivine-Orthopyroxene-Spinel Oxygen Geobarometer: Implications for the Oxidation State of the Upper Mantle. *Contr. Mineral. Pet.* 107, 27–40. doi:10.1007/bf00311183
- Beattie, P. (1993). Olivine-melt and Orthopyroxene-Melt Equilibria. *Contr. Mineral. Pet.* 115, 103–111. doi:10.1007/bf00712982
- Bédard, J. H. (1999). Petrogenesis of Boninites from the Betts Cove Ophiolite, Newfoundland, Canada: Identification of Subducted Source Components. *J. Petrology* 40, 1853–1889. doi:10.1093/ptro/40.12.1853
- Bédard, J. H. (2007). Trace Element Partitioning Coefficients between Silicate Melts and Orthopyroxene: Parameterizations of D Variations. *Chem. Geol.* 244, 263–303. doi:10.1016/j.chemgeo.2007.06.019
- Behrens, H., Roux, J., Neuville, D. R., and Siemann, M. (2006). Quantification of Dissolved H<sub>2</sub>O in Silicate Glasses Using Confocal microRaman Spectroscopy. *Chem. Geol.* 229, 96–112. doi:10.1016/j.chemgeo.2006.01.014
- Bénard, A., Arculus, R. J., Nebel, O., Ionov, D. A., and McAlpine, S. R. B. (2017b). Silica-enriched Mantle Sources of Subalkaline Picrite-Boninite-Andesite Island Arc Magmas. *Geochimica Cosmochimica Acta* 199, 287–303. doi:10.1016/j.gca.2016.09.030
- Bénard, A., and Ionov, D. A. (2012). A New Petrogenetic Model for Low-Ca Boninites: Evidence from Veined Sub-arc Xenoliths on Melt-Mantle Interaction and Melt Fractionation. *Geochem. Geophys. Geosyst.* 13, Q0AF05. doi:10.1029/2012GC004145
- Bénard, A., and Ionov, D. A. (2013). Melt- and Fluid-Rock Interaction in Supra-subduction Lithospheric Mantle: Evidence from Andesite-Hosted Veined Peridotite Xenoliths. *J. Pet.* 54, 2339–2378. doi:10.1093/ptrology/egt050
- Bénard, A., Klimm, K., Woodland, A. B., Arculus, R. J., Wilke, M., Botcharnikov, R. E., et al. (2018c). Oxidising Agents in Sub-arc Mantle Melts Link Slab Devolatilisation and Arc Magmas. *Nat. Commun.* 9, 3500. doi:10.1038/s41467-018-05804-2
- Bénard, A., Koga, K. T., Shimizu, N., Kendrick, M. A., Ionov, D. A., Nebel, O., et al. (2017a). Chlorine and Fluorine Partition Coefficients and Abundances in Sub-arc Mantle Xenoliths (Kamchatka, Russia): Implications for Melt Generation and Volatile Recycling Processes in Subduction Zones. *Geochimica Cosmochimica Acta* 199, 324–350. doi:10.1016/j.gca.2016.10.035
- Bénard, A., Le Losq, C., Nebel, O., and Arculus, R. J. (2018a). Low-Ca Boninite Formation by Second-Stage Melting of Spinel Harzburgite Residues at Mature Subduction Zones: New Evidence from Veined Mantle Xenoliths from the West Bismarck Arc. *Contrib. Mineral. Pet.* 173, 105. doi:10.1007/s00410-018-1526-6
- Bénard, A., Müntener, O., Pilet, S., Arculus, R. J., and Nebel, O. (2021). Silica-rich Spinel Harzburgite Residues Formed by Fractional Hybridization-Melting of the Intra-oceanic Supra-subduction Zone Mantle: New Evidence from TUBAF Seamount Peridotites. *Geochimica Cosmochimica Acta* 293, 477–506. doi:10.1016/j.gca.2020.11.001
- Bénard, A., Nebel, O., Ionov, D. A., Arculus, R. J., Shimizu, N., and Métrich, N. (2016). Primary Silica-Rich Picrite and High-Ca Boninite Melt Inclusions in Pyroxenite Veins from the Kamchatka Sub-arc Mantle. *J. Petrol.* 57, 1955–1982. doi:10.1093/ptrology/egw066
- Bénard, A., Palle, S., Doucet, L. S., and Ionov, D. A. (2011). Three-dimensional Imaging of Sulfides in Silicate Rocks at Submicron Resolution with Multiphoton Microscopy. *Microsc. Microanal.* 17, 937–943. doi:10.1017/s1431927611011883
- Bénard, A., Woodland, A. B., Arculus, R. J., Nebel, O., and McAlpine, S. R. B. (2018b). Variation in Sub-arc Mantle Oxygen Fugacity during Partial Melting Recorded in Refractory Peridotite Xenoliths from the West Bismarck Arc. *Chem. Geol.* 486, 16–30. doi:10.1016/j.chemgeo.2018.03.004
- Botcharnikov, R. E., Linnen, R. L., Wilke, M., Holtz, F., Jugo, P. J., and Berndt, J. (2011). High Gold Concentrations in Sulphide-Bearing Magma under Oxidizing Conditions. *Nat. Geosci.* 4, 112–115. doi:10.1038/NGEO1042
- Brenan, J. M., Shaw, H. F., Ryerson, F. J., and Phinney, D. L. (1995). Experimental Determination of Trace-Element Partitioning between Pargasite and a Synthetic Hydrous Andesitic Melt. *Earth Planet. Sci. Lett.* 135, 1–11. doi:10.1016/0012-821x(95)00139-4
- Brey, G. P., and Köhler, T. (1990). Geothermobarometry in Four-phase Lherzolites II. New Thermobarometers, and Practical Assessment of Existing Thermobarometers. *J. Petrology* 31, 1353–1378. doi:10.1093/ptrology/31.6.1353
- Cameron, W. E., McCulloch, M. T., and Walker, D. A. (1983). Boninite Petrogenesis: Chemical and Nd-Sr Isotopic Constraints. *Earth Planet. Sci. Lett.* 65, 75–89. doi:10.1016/0012-821x(83)90191-7
- Craig, J. R., and Kullerud, G. (1969). Phase Relations in the Fe-Ni-Cu-S System and Their Application to Magmatic Ore Deposits. *Econ. Geol.* 4, 344–358.
- Crawford, A. J., Falloon, T. J., and Green, D. H. (1989). “Classification, Petrogenesis and Tectonic Setting of Boninites,” in *Boninites and Related Rocks*. Editor A. J. Crawford (London: Unwin Hyman), 1–49.
- Dalou, C., Koga, K. T., Le Voyer, M., and Shimizu, N. (2014). Contrasting Partition Behavior of F and Cl during Hydrous Mantle Melting: Implications for Cl/F Signature in Arc Magmas. *Prog. Earth Planet. Sci.* 1, 26–42. doi:10.1186/s40645-014-0026-1
- Dalou, C., Le Losq, C., Mysen, B. O., and Cody, G. D. (2015). Solubility and Solution Mechanisms of Chlorine and Fluorine in Aluminosilicate Melts at High Pressure and High Temperature. *Am. Mineralogist* 100, 2272–2283. doi:10.2138/am-2015-5201
- Dalou, C., and Mysen, B. O. (2015). The Effect of H<sub>2</sub>O on F and Cl Solubility and Solution Mechanisms of in Aluminosilicate Melts at High Pressure and High Temperature. *Am. Mineralogist* 100, 633–643. doi:10.2138/am-2015-4814
- Dobson, P. F., Blank, J. G., Maruyama, S., and Liou, J. G. (2006). Petrology and Geochemistry of Boninite-Series Volcanic Rocks, Chichi-Jima, Bonin Islands, Japan. *Int. Geol. Rev.* 48, 669–701. doi:10.2747/0020-6814.48.8.669
- Dobson, P. F., Skogby, H., and Rossman, G. R. (1995). Water in Boninite Glass and Coexisting Orthopyroxene: Concentration and Partitioning. *Contrib. Mineral. Pet.* 118, 414–419. doi:10.1007/s004100050023
- Duncan, R. A., and Green, D. H. (1987). The Genesis of Refractory Melts in the Formation of Oceanic Crust. *Contrib. Mineral. Pet.* 96, 326–342. doi:10.1007/bf00371252
- Edgar, A. D., and Pizzolato, L. A. (1995). An Experimental Study of Partitioning of Fluorine between K-Richterite, Apatite, Phlogopite, and Melt at 20 Kbar. *Contrib. Mineral. Pet.* 121, 247–257. doi:10.1007/bf02688240
- Falloon, T. J., and Danyushevsky, L. V. (2000). Melting of Refractory Mantle at 1.5, 2 and 2.5 GPa under Anhydrous and H<sub>2</sub>O-Undersaturated Conditions: Implications for the Petrogenesis of High-Ca Boninites and the Influence of Subduction Components on Mantle Melting. *J. Pet.* 41, 257–283. doi:10.1093/ptrology/41.2.257
- Fleet, M. E., Chryssoulis, S. L., Stone, W. E., and Weisener, C. G. (1993). Partitioning of Platinum-Group Elements and Au in the Fe-Ni-Cu-S System: Experiments on the Fractional Crystallization of Sulfide Melt. *Contrib. Mineral. Pet.* 115, 36–44. doi:10.1007/bf00712976
- Fleet, M. E., and Pan, Y. (1994). Fractional Crystallization of Anhydrous Sulfide Liquid in the System Fe-Ni-Cu-S, with Application to Magmatic Sulfide Deposits. *Geochimica Cosmochimica Acta* 58, 3369–3377. doi:10.1016/0016-7037(94)90092-2
- Flemetakis, S., Klemme, S., Stracke, A., Genske, F., Berndt, J., and Rohrbach, A. (2021). Constraining the Presence of Amphibole and Mica in Metasomatized Mantle Sources through Halogen Partitioning Experiments. *Lithos* 380–381, 105859. doi:10.1016/j.lithos.2020.105859
- Fonseca, R. O. C., Campbell, I. H., O'Neill, H. S. C., and Fitzgerald, J. D. (2008). Oxygen Solubility and Speciation in Sulphide-Rich Mattes. *Geochimica Cosmochimica Acta* 72, 2619–2635. doi:10.1016/j.gca.2008.03.009
- Gao, S., Liu, X., Yuan, H., Hattendorf, B., Günther, D., Chen, L., et al. (2002). Determination of Forty Two Major and Trace Elements in USGS and NIST SRM Glasses by Laser Ablation-Inductively Coupled Plasma-Mass Spectrometry. *Geostand. Geoanal. Res.* 26, 181–196. doi:10.1111/j.1751-908x.2002.tb00886.x
- Ghiorso, M. S., Hirschmann, M. M., Reiners, P. W., and Kress, V. C. (2002). The pMELTS: A Revision of MELTS for Improved Calculation of Phase Relations and Major Element Partitioning Related to Partial Melting of the Mantle to 3 GPa. *Geochem.-Geophys.-Geosyst.* 3, 1–35. doi:10.1029/2001GC000217
- Grant, T. B., Harlov, D. E., and Rhede, D. (2016). Experimental Formation of Pyroxenite Veins by Reactions between Olivine and Si, Al, Ca, Na, and Cl-Rich Fluids at 800°C and 800 MPa: Implications for Fluid Metasomatism in the Mantle Wedge. *Am. Mineralogist* 101, 808–818. doi:10.2138/am-2016-5441

- Hamlyn, P. R., and Keays, R. R. (1986). Sulfur Saturation and Second-Stage Melts; Application to the Bushveld Platinum Metal Deposits. *Econ. Geol.* 81, 1431–1445. doi:10.2113/gsecongeo.81.6.1431
- Hauri, E., Gaetani, G., and Green, T. (2006). Partitioning of Water during Melting of the Earth's Upper Mantle at H<sub>2</sub>O-Undersaturated Conditions. *Earth Planet. Sci. Lett.* 248, 715–734. doi:10.1016/j.epsl.2006.06.014
- Hickey, R. L., and Frey, F. A. (1982). Geochemical Characteristics of Boninite Series Volcanics: Implications for Their Source. *Geochimica Cosmochimica Acta* 46, 2099–2115. doi:10.1016/0016-7037(82)90188-0
- Ionov, D. A., Bénard, A., and Plechov, P. Y. (2011). Melt Evolution in Subarc Mantle: Evidence from Heating Experiments on Spinel-Hosted Melt Inclusions in Peridotite Xenoliths from the Andesitic Avacha Volcano (Kamchatka, Russia). *Contrib. Mineral. Pet.* 162, 1159–1174. doi:10.1007/s00410-011-0645-0
- Ionov, D. A., Bénard, A., Plechov, P. Y., and Shcherbakov, V. D. (2013). Along-arc Variations in Lithospheric Mantle Compositions in Kamchatka, Russia: First Trace Element Data on Mantle Xenoliths from the Klyuchevskoy Group Volcanoes. *J. Volcanol. Geotherm. Res.* 263, 122–131. doi:10.1016/j.jvolgeores.2012.12.022
- Ionov, D. A. (2010). Petrology of Mantle Wedge Lithosphere: New Data on Supra-subduction Zone Peridotite Xenoliths from the Andesitic Avacha Volcano, Kamchatka. *J. Pet.* 51, 327–361. doi:10.1093/petrology/egp090
- Ishimaru, S., Arai, S., Ishida, Y., Shirasaka, M., and Okrugin, V. M. (2007). Melting and Multi-Stage Metasomatism in the Mantle Wedge beneath a Frontal Arc Inferred from Highly Depleted Peridotite Xenoliths from the Avacha Volcano, Southern Kamchatka. *J. Pet.* 48, 395–433. doi:10.1093/petrology/egl065
- Ishimaru, S., and Arai, S. (2008). Calcic Amphiboles in Peridotite Xenoliths from Avacha Volcano, Kamchatka, and Their Implications for Metasomatic Conditions in the Mantle Wedge. *Geol. Soc. Lond. Spec. Publ.* 293, 35–55. doi:10.1144/sp293.3
- Jarosewich, E., Nelen, J. A., and Norberg, J. A. (1980). Reference Samples for Electron Microprobe Analysis\*. *Geostand. Geoanal. Res.* 4, 43–47. doi:10.1111/j.1751-908x.1980.tb00273.x
- Jenner, G. A. (1981). Geochemistry of High-Mg Andesites from Cape Vogel, Papua New Guinea. *Chem. Geol.* 33, 307–332. doi:10.1016/0009-2541(81)90106-6
- Jochum, K. P., Weis, U., Stoll, B., Kuzmin, D., Yang, Q., Raczek, I., et al. (2011). Determination of Reference Values for NIST SRM 610-617 Glasses Following ISO Guidelines. *Geostand. Geoanal. Res.* 35, 397–429. doi:10.1111/j.1751-908x.2011.00120.x
- Jochum, K. P., Willbold, M., Raczek, I., Stoll, B., and Herwig, K. (2005). Chemical Characterisation of the USGS Reference Glasses GSA-1G, GSC-1G, GSD-1G, GSE-1G, BCR-2G, BHVO-2G and BIR-1G Using EPMA, ID-TIMS, ID-ICP-MS and LA-ICP-MS. *Geostand. Geoanal. Res.* 29, 285–302. doi:10.1111/j.1751-908x.2005.tb00901.x
- Jugo, P. J., Wilke, M., and Botcharnikov, R. E. (2010). Sulfur K-Edge XANES Analysis of Natural and Synthetic Basaltic Glasses: Implications for S Speciation and S Content as Function of Oxygen Fugacity. *Geochimica Cosmochimica Acta* 74, 5926–5938. doi:10.1016/j.gca.2010.07.022
- Kamenetsky, V. S., Sobolev, A. V., Eggins, S. M., Crawford, A. J., and Arculus, R. J. (2002). Olivine-enriched Melt Inclusions in Chromites from Low-Ca Boninites, Cape Vogel, Papua New Guinea: Evidence for Ultramafic Primary Magma, Refractory Mantle Source and Enriched Components. *Chem. Geol.* 183, 287–303. doi:10.1016/s0009-2541(01)00380-1
- Keays, R. R. (1995). The Role of Komatiitic and Picritic Magmatism and S-Saturation in the Formation of Ore Deposits. *Lithos* 34, 1–18. doi:10.1016/0024-4937(95)90003-9
- Kelemen, P. B., Hanghøj, K., and Greene, A. R. (2014). “One View of the Geochemistry of Subduction-Related Magmatic Arcs, with an Emphasis on Primitive Andesite and Lower Crust,” in *Treatise on Geochemistry*. Editors H. Holland and K. Turekian. 2nd edn. (Amsterdam: Elsevier), 1–70. doi:10.1016/b978-0-08-095975-7.00323-5
- Klein, M., Stosch, H.-G., and Seck, H. A. (1997). Partitioning of High Field-Strength and Rare-Earth Elements between Amphibole and Quartz-Dioritic to Tonalitic Melts: an Experimental Study. *Chem. Geol.* 138, 257–271. doi:10.1016/s0009-2541(97)00019-3
- Klimm, K., Kohn, S. C., and Botcharnikov, R. E. (2012). The Dissolution Mechanism of Sulphur in Silicate Melts. II: Solubility and Speciation of Sulphur in Silicate Melts as a Function of *f*O<sub>2</sub>. *Chem. Geol.* 322–323, 250–267. doi:10.1016/j.chemgeo.2012.04.028
- Klingenberg, B. M. E. T., and Kushiro, I. (1996). Melting of a Chromite-Bearing Harzburgite and Generation of Boninitic Melts at Low Pressures under Controlled Oxygen Fugacity. *Lithos* 37, 1–14. doi:10.1016/0024-4937(95)00025-9
- Komatsu, M. (1980). Clinostatite in Volcanic Rocks from the Bonin Islands. *Contr. Mineral. Pet.* 74, 329–338. doi:10.1007/bf00518114
- König, S., Münker, C., Schuth, S., Luguet, A., Hoffmann, J. E., and Kuduon, J. (2010). Boninites as Windows into Trace Element Mobility in Subduction Zones. *Geochimica Cosmochimica Acta* 74, 684–704. doi:10.1016/j.gca.2009.10.011
- Kress, V. C., and Carmichael, I. S. E. (1991). The Compressibility of Silicate Liquids Containing Fe<sub>2</sub>O<sub>3</sub> and the Effect of Composition, Temperature, Oxygen Fugacity and Pressure on Their Redox States. *Contr. Mineral. Pet.* 108, 82–92. doi:10.1007/bf00307328
- Kullerød, G., Yund, R. A., and Moh, G. H. (1969). Phase Relation in the Cu-Fe-Ni, Cu-Ni-S and Fe-Ni-S Systems. *Econ. Geol.* 4, 323–343.
- Kushiro, I. (1982). Petrology of High-MgO Bronzite Andesite Resembling Boninite from Site 458 Near the Mariana Trench. *Init. Rep. Deep Sea Drill. Proj.* 60, 731–735. doi:10.2973/dsdp.proc.60.139.1982
- Le Bas, M. J. (2000). IUGS Reclassification of the High-Mg and Picritic Volcanic Rocks. *J. Pet.* 41, 1467–1470. doi:10.1093/petrology/41.10.1467
- Le Losq, C. (2018). Rampy: a Python Library for Processing Spectroscopic (IR, Raman, XAS) Data. *Zenodo*. doi:10.5281/zenodo.1168729
- Le Losq, C., Dalou, C., and Mysen, B. O. (2017). *In Situ* study at High Pressure and Temperature of the Environment of Water in Hydrous Na and Ca Aluminosilicate Melts and Coexisting Aqueous Fluids. *J. Geophys. Res. Solid Earth* 122, 4888–4899. doi:10.1002/2017JB014262
- Le Losq, C., Neuville, D. R., Moretti, R., and Roux, J. (2012). Determination of Water Content in Silicate Glasses Using Raman Spectrometry: Implications for the Study of Explosive Volcanism. *Am. Mineralogist* 97, 779–790. doi:10.2138/am.2012.3831
- L'Heureux, I., and Fowler, A. D. (1996). Isothermal Constitutive Undercooling as a Model for Oscillatory Zoning in Plagioclase. *Can. Mineral.* 34, 1137–1147.
- Li, H.-Y., Li, X., Ryan, J. G., Zhang, C., and Xu, Y.-G. (2022). Boron Isotopes in Boninites Document Rapid Changes in Slab Inputs during Subduction Initiation. *Nat. Commun.* 13, 993. doi:10.1038/s41467-022-28637-6
- London, D., and Morgan, G. B. (2012). The Pegmatite Puzzle. *Elements* 8, 263–268. doi:10.2113/gselements.8.4.263
- Longerich, H. P., Jackson, S. E., and Günther, D. (1996). Inter-laboratory Note. Laser Ablation Inductively Coupled Plasma Mass Spectrometric Transient Signal Data Acquisition and Analyte Concentration Calculation. *J. Anal. At. Spectrom.* 11, 899–904. doi:10.1039/ja9961100899
- Lorand, J. P. (1990). Are Spinel Iherzolite Xenoliths Representative of the Abundance of Sulfur in the Upper Mantle? *Geochimica Cosmochimica Acta* 54, 1487–1492. doi:10.1016/0016-7037(90)90173-i
- Mallmann, G., and O'Neill, H. S. C. (2009). The Crystal/melt Partitioning of V during Mantle Melting as a Function of Oxygen Fugacity Compared with Some Other Elements (Al, P, Ca, Sc, Ti, Cr, Fe, Ga, Y, Zr and Nb). *J. Pet.* 50, 1765–1794. doi:10.1093/petrology/egp053
- Mandler, B. E., and Grove, T. L. (2016). Controls on the Stability and Composition of Amphibole in the Earth's Mantle. *Contrib. Mineral. Pet.* 171, 68. doi:10.1007/s00410-016-1281-5
- Matjuschkin, V., Blundy, J. D., and Brooker, R. A. (2016). The Effect of Pressure on Sulphur Speciation in Mid- to Deep-Crustal Arc Magmas and Implications for the Formation of Porphyry Copper Deposits. *Contrib. Mineral. Pet.* 171, 66. doi:10.1007/s00410-016-1274-4
- Mavrogenes, J. A., and O'Neill, H. S. C. (1999). The Relative Effects of Pressure, Temperature and Oxygen Fugacity on the Solubility of Sulfide in Mafic Magmas. *Geochimica Cosmochimica Acta* 63, 1173–1180. doi:10.1016/s0016-7037(98)00289-0
- McDade, P., Blundy, J. D., and Wood, B. J. (2003). Trace Element Partitioning Between Mantle Wedge Peridotite and Hydrous MgO-Rich Melt. *Am. Mineralogist* 88 (11–12), 1825–1831. doi:10.2138/am-2003-11-1225
- McDonough, W. F., and Sun, S.-s. (1995). The Composition of the Earth. *Chem. Geol.* 120, 223–253. doi:10.1016/0009-2541(94)00140-4
- McInnes, B. I. A., Gregoire, M., Binns, R. A., Herzog, P. M., and Hannington, M. D. (2001). Hydrous Metasomatism of Oceanic Sub-arc Mantle, Lihir, Papua New Guinea: Petrology and Geochemistry of Fluid-Metasomatised Mantle Wedge

- Xenoliths. *Earth Planet. Sci. Lett.* 188, 169–183. doi:10.1016/s0012-821x(01)00306-5
- Moretti, R., and Baker, D. R. (2008). Modeling the Interplay of  $f_{O_2}$  and  $f_{S_2}$  along the Fe-Silicate Melt Equilibrium. *Chem. Geol.* 256, 286–298. doi:10.1016/j.chemgeo.2008.06.055
- Mungall, J. E. (2002). Empirical Models Relating Viscosity and Tracer Diffusion in Magmatic Silicate Melts. *Geochimica Cosmochimica Acta* 66, 125–143. doi:10.1016/s0016-7037(01)00736-0
- Mysen, B. O., and Wheeler, K. (2000). Solubility Behavior of Water in Haploandesitic Melts at High Pressure and High Temperature. *Am. Mineralogist* 85, 1128–1142. doi:10.2138/am-2000-8-903
- Nandedkar, R. H., Hürllimann, N., Ulmer, P., and Müntener, O. (2016). Amphibole-melt Trace Element Partitioning of Fractionating Calc-Alkaline Magmas in the Lower Crust: an Experimental Study. *Contrib. Mineral. Pet.* 171, 71. doi:10.1007/s00410-016-1278-0
- Nikolaev, G. S., Ariskin, A. A., and Barmina, G. S. (2018). SPINMELT-2.0: Simulation of Spinel-Melt Equilibrium in Basaltic Systems under Pressures up to 15 Kbar: I. Model Formulation, Calibration, and Tests. *Geochem. Int.* 56, 24–45. doi:10.1134/s0016702918010044
- O'Neill, H. St. C., and Mavrogenes, J. A. (2002). The Sulfide Capacity and the Sulfur Content at Sulfide Saturation of Silicate Melts at 1400°C and 1 Bar. *J. Pet.* 43, 1049–1087. doi:10.1093/petrology/43.6.1049
- O'Neill, H. St. C., and Wall, V. J. (1987). The Olivine-Orthopyroxene-Spinel Oxygen Geobarometer, the Nickel Precipitation Curve, and the Oxygen Fugacity of the Earth's Upper Mantle. *J. Pet.* 28, 1169–1191.
- Parman, S. W., and Grove, T. L. (2004). Harzburgite Melting with and without H<sub>2</sub>O: Experimental Data and Predictive Modelling. *J. Geophys. Res.* 109, B02201. doi:10.1029/2003JB002566
- Pearce, J. A., and Arculus, R. J. (2021). “Boninites,” in *Encyclopedia of Geology*. Editors D. Alderton and S. A. Elias. 2nd edn. (Amsterdam: Elsevier), 113–129. doi:10.1016/b978-0-08-102908-4.00152-1
- Pearce, J. A., Kempton, P. D., Nowell, G. M., and Noble, S. R. (1999). Hf-Nd Element and Isotope Perspective of the Nature and Provenance of Mantle and Subduction Components in Western Pacific Arc-Basin Systems. *J. Petrology* 40, 1579–1611. doi:10.1093/ptrology/40.11.1579
- Pearce, J. A., and Reagan, M. K. (2019). Identification, Classification, and Interpretation of Boninites from Anthropocene to Eoarchean Using Si-Mg-Ti Systematics. *Geosphere* 15, 1008–1037. doi:10.1130/ges01661.1
- Putirka, K. D. (2008). 3. Thermometers and Barometers for Volcanic Systems. *Rev. Mineralogy Geochem.* 69, 61–120. Putirka KD, Tepley FJ (eds) Minerals, Inclusions and Volcanic Processes. doi:10.1515/9781501508486-004
- Reagan, M. K., Ishizuka, O., Stern, R. J., Kelley, K. A., Ohara, Y., Blichert-Toft, J., et al. (2010). Fore-arc Basalts and Subduction Initiation in the Izu-Bonin-Mariana System. *Geochem. Geophys. Geosyst.* 11, Q03X12. doi:10.1029/2009GC002871
- Saal, A. E., Hauri, E. H., Langmuir, C. H., and Perfit, M. R. (2002). Vapour Undersaturation in Primitive Mid-ocean-ridge Basalt and the Volatile Content of Earth's Upper Mantle. *Nature* 419, 451–455. doi:10.1038/nature01073
- Salters, V. J. M., and Stracke, A. (2004). Composition of the Depleted Mantle. *Geochem. Geophys. Geosyst.* 5, Q05B07. doi:10.1029/2003GC000597
- Schiavi, F., Bolfan-Casanova, N., Withers, A. C., Médard, E., Laumonier, M., Laporte, D., et al. (2018). Water Quantification in Silicate Glasses by Raman Spectroscopy: Correcting for the Effects of Confocality, Density and Ferric Iron. *Chem. Geol.* 483, 312–331. doi:10.1016/j.chemgeo.2018.02.036
- Shea, T., and Hammer, J. E. (2013). Kinetics of Cooling- and Decompression-Induced Crystallization in Hydrous Mafic-Intermediate Magmas. *J. Volcanol. Geotherm. Res.* 260, 127–145. doi:10.1016/j.jvolgeores.2013.04.018
- Shimizu, H., Sawatari, H., Kawata, Y., Dunkley, P. N., and Masuda, A. (1992). Ce and Nd Isotope Geochemistry on Island Arc Volcanic Rocks with Negative Ce Anomaly: Existence of Sources with Concave REE Patterns in the Mantle beneath the Solomon and Bonin Island Arcs. *Contr. Mineral. Pet.* 110, 242–252. doi:10.1007/bf00310741
- Smythe, D. J., Wood, B. J., and Kiseeva, E. S. (2017). The S Content of Silicate Melts at Sulfide Saturation: New Experiments and a Model Incorporating the Effects of Sulfide Composition. *Am. Mineralogist* 102, 795–803. doi:10.2138/am-2017-5800ccby
- Sobolev, A. V., and Chaussidon, M. (1996). H<sub>2</sub>O Concentrations in Primary Melts from Supra-subduction Zones and Mid-ocean Ridges: Implications for H<sub>2</sub>O Storage and Recycling in the Mantle. *Earth Planet. Sci. Lett.* 137, 45–55. doi:10.1016/0012-821x(95)00203-0
- Soustelle, V., Tommasi, A., Demouchy, S., and Ionov, D. A. (2010). Deformation and Fluid-Rock Interaction in the Supra-subduction Mantle: Microstructures and Water Contents in Peridotite Xenoliths from the Avacha Volcano, Kamchatka. *J. Petrology* 51, 363–394. doi:10.1093/petrology/egp085
- Taylor, R. N., Nesbitt, R. W., Vidal, P., Harmon, R. S., Auvray, B., and Croudace, I. W. (1994). Mineralogy, Chemistry, and Genesis of the Boninite Series Volcanics, Chichijima, Bonin Islands, Japan. *J. Petrology* 35, 577–617. doi:10.1093/petrology/35.3.577
- Tollan, P. M. E., Dale, C. W., Hermann, J., Davidson, J. P., and Arculus, R. J. (2017). Generation and Modification of the Mantle Wedge and Lithosphere beneath the West Bismarck Island Arc: Melting, Metasomatism and Thermal History of Peridotite Xenoliths from Ritter Island. *J. Pet.* 58, 1475–1510. doi:10.1093/petrology/egx062
- Umino, S., and Kushiro, I. (1989). “Experimental Studies on Boninite Petrogenesis,” in *Boninites and Related Rocks*. Editor A. J. Crawford (London: Unwin Hyman), 89–111.
- Umino, S., Kitamura, K., Kanayama, K., Tamura, A., Sakamoto, N., Ishizuka, O., et al. (2015). Thermal and Chemical Evolution of the Subarc Mantle Revealed by Spinel-Hosted Melt Inclusions in Boninite from the Ogasawara (Bonin) Archipelago, Japan. *Geology* 43, 151–154. doi:10.1130/g36191.1
- Umino, S. (1986). Magma Mixing in Boninite Sequence of Chichijima, Bonin Islands. *J. Volcanol. Geotherm. Res.* 29, 125–157. doi:10.1016/0377-0273(86)90042-9
- Urann, B. M., Le Roux, V., Hammond, K., Marschall, H. R., Lee, C.-T. A., and Monteleone, B. D. (2017). Fluorine and Chlorine in Mantle Minerals and the Halogen Budget of the Earth's Mantle. *Contrib. Mineral. Pet.* 172, 51. doi:10.1007/s00410-017-1368-7
- Valetich, M. J., Le Losq, C., Arculus, R. J., Umino, S., and Mavrogenes, J. (2021). Compositions and Classification of Fractionated Boninite Series Melts from the Izu-Bonin-Mariana Arc: a Machine Learning Approach. *J. Pet.* 62 (2), egab013. doi:10.1093/petrology/egab013
- Van den Bleeken, G., and Koga, K. T. (2015). Experimentally Determined Distribution of Fluorine and Chlorine upon Hydrous Slab Melting, and Implications for F-Cl Cycling through Subduction Zones. *Geochimica Cosmochimica Acta* 171, 353–373. doi:10.1016/j.gca.2015.09.030
- Venugopal, S., Schiavi, F., Moune, S., Bolfan-Casanova, N., Druitt, T., and Williams-Jones, G. (2020). Melt Inclusion Vapour Bubbles: the Hidden Reservoir for Major and Volatile Elements. *Sci. Rep.* 10, 9034. doi:10.1038/s41598-020-65226-3
- Waters, L. E., and Lange, R. A. (2017). An Experimental Study of  $^{Fe^{2+}-Mg}K_D$  between Orthopyroxene and Rhyolite: a Strong Dependence on H<sub>2</sub>O in the Melt. *Contrib. Mineral. Pet.* 172, 42. doi:10.1007/s00410-017-1358-9
- Watson, E. B., and Müller, T. (2009). Non-equilibrium Isotopic and Elemental Fractionation during Diffusion-Controlled Crystal Growth under Static and Dynamic Conditions. *Chem. Geol.* 267, 111–124. doi:10.1016/j.chemgeo.2008.10.036
- Watson, E. B. (1996). Surface Enrichment and Trace-Element Uptake during Crystal Growth. *Geochimica Cosmochimica Acta* 60, 5013–5020. doi:10.1016/s0016-7037(96)00299-2
- Webster, J. D. (1997b). Chloride Solubility in Felsic Melts and the Role of Chloride in Magmatic Degassing. *J. Petrology* 38, 1793–1807. doi:10.1093/ptrology/38.12.1793
- Webster, J. D. (1997a). Exsolution of Magmatic Volatile Phases from Cl-Enriched Mineralizing Granitic Magmas and Implications for Ore Metal Transport. *Geochimica Cosmochimica Acta* 61, 1017–1029. doi:10.1016/s0016-7037(96)00395-x
- Webster, J. D., Kinzler, R. J., and Mathez, E. A. (1999). Chloride and Water Solubility in Basalt and Andesite Melts and Implications for Magmatic

- Degassing. *Geochimica Cosmochimica Acta* 63, 729–738. doi:10.1016/s0016-7037(99)00043-5
- Wood, B. J., and Blundy, J. D. (1997). A Predictive Model for Rare Earth Element Partitioning between Clinopyroxene and Anhydrous Silicate Melt. *Contributions Mineralogy Petrology* 129, 166–181. doi:10.1007/s004100050330
- Wood, B. J., Bryndzia, L. T., and Johnson, K. E. (1990). Mantle Oxidation State and its Relationship to Tectonic Environment and Fluid Speciation. *Science* 248, 337–345. doi:10.1126/science.248.4953.337
- Yajima, K., Fujimaki, H., and Kuroda, N. (2001). Primitive Tholeiites and Calc-Alkaline Rocks from Hahajima, Bonin (Ogasawara) Archipelago. *Jpn. Mag. Mineralogical Petrological Sci.* 30, 164–179. doi:10.2465/gkk.30.164
- Zajacz, Z., Candela, P. A., Piccoli, P. M., and Sanchez-Valle, C. (2012). The Partitioning of Sulfur and Chlorine between Andesite Melts and Magmatic Volatiles and the Exchange Coefficients of Major Cations. *Geochimica Cosmochimica Acta* 89, 81–101. doi:10.1016/j.gca.2012.04.039
- Zhang, Z., and Hirschmann, M. M. (2016). Experimental Constraints on Mantle Sulfide Melting up to 8 GPa. *Am. Mineralogist* 101, 181–192. doi:10.2138/am-2016-5308
- Conflict of Interest:** The authors declare that the research was conducted in the absence of any commercial or financial relationships that could be construed as a potential conflict of interest.
- Publisher's Note:** All claims expressed in this article are solely those of the authors and do not necessarily represent those of their affiliated organizations, or those of the publisher, the editors, and the reviewers. Any product that may be evaluated in this article, or claim that may be made by its manufacturer, is not guaranteed or endorsed by the publisher.
- Copyright © 2022 Bénard, Le Losq, Müntener, Robyr, Nebel, Arculus and Ionov. This is an open-access article distributed under the terms of the Creative Commons Attribution License (CC BY). The use, distribution or reproduction in other forums is permitted, provided the original author(s) and the copyright owner(s) are credited and that the original publication in this journal is cited, in accordance with accepted academic practice. No use, distribution or reproduction is permitted which does not comply with these terms.